Development of Advanced Thin Films by PECVD for Photovoltaic Applications

by

Lin Tian

A thesis
presented to the University of Waterloo
in fulfillment of the
thesis requirement for the degree of
Master of Applied Science
in
Electrical and Computer Engineering

Waterloo, Ontario, Canada, 2013

AUTHOR'S DECLARATION

I hereby declare that I am the sole author of this thesis. This is a true copy of the thesis, including any required final revisions, as accepted by my examiners.

I understand that my thesis may be made electronically available to the public.

Abstract

Compared to wafer based solar cells, thin film solar cells greatly reduce material cost and thermal budget due to low temperature process. Monolithically manufacturing allows large area fabrication and continuous processing. In this work, several photovoltaic thin films have been developed by rf-PECVD including a-Si:H and μc-Si, both intrinsic and doped on Corning 4 inch glass substrate at low temperature. The conductivity of n type and p type μc-Si at 180ºC was 17S/cm and 7.1E-2S/cm, respectively. B dopants either in a-Si:H or μc-Si films require higher plasma power to get active doping. The B_2H_6-to-SiH_4 flow ratio for p type μc-Si lies from 0.01 to 0.025. Chamber conditions have critical effect on film quality. Repeatable and superior results require a well-established cleaning passivation procedure.

Moreover, μc-Si films have been deposited from pure silane on glass substrate by modified rf-ICP-CVD. The deposition rate has been dramatically increased to 5Å/s due to little H_2 dilution with crystalline fraction was around 69%, and 6.2Å/s with crystalline fraction 45%. Microstructure started to form at 150ºC with a thin incubation layer on the glass substrate, and became fully dense conical conglomerates around 300nm where conductivity and crystallinity saturated. Additionally, a-SiGe:H films have been developed by modified rf-ICP-CVD. The optical band gaps have been varied from 1.25 to 1.63eV by changing SiH_4-to-GeH_4 ratio. Also high temperature resulted in low bandgap. Cross-section TEM showed some microcrystllites appeared near interface region. Heterojunction solar cells on p type c-Si wafer have been fabricated using films developed in this thesis. Interference fringes in EQE disappeared on either textured substrate or cells with lift-off contacts. Maximum EQE was 87% around 700nm. I-V curves have also been studied where the interesting kink suggests a counter-diode has formed between emitter region and contacts.

Acknowledgements

I wish to sincerely express my gratitude to:

Professor Siva Sivoththaman for his far-sight guidance and kind support during the last two years;

I am deeply grateful to Dr. Ehsanollah Fathi for his patient guidance and excellent advice throughout this study;

I owe my sincere gratitude to Roohen S.Tarighat for his extensive discussions and constructive comments;

I wish to express my warm and sincere thanks to Joseph Street for his valuable efforts in CAPDS lab;

I would like to express my gratitude to my colleagues Zhen Gao, Nasim Bakhshi Zadeh, Dr. Bahareh Sadeghimakki, Maziar Moradi, Behzad Esfandiarpour, Navid Jahed, Mohsen Mahmoudysepehr, Shadi Dashmiz, Christopher Baldus-Jeursen, Bita Janfeshan for precious cooperation and unforgettable time we spent in CAPDS.

My special gratitude goes to my boyfriend, Zheng Han, for his deep love, consistent support and help. And finally I would like to express my profound gratitude to my beloved parents for all their support.

Table of Contents

List of Figures

Chapter 1

Introduction

1.1 Overview of Solar Cells

How to meet world's energy needs in a sustainable and affordable way has been a hot issue after oil price soared up which is only a matter of time before it surges again. Moreover, the Fukushima nuclear accident in 2011, clouded the outlook of nuclear electricity generation, some countries have announced not to restart or to terminate nuclear gradually within the next 10 to 25 years.

Meanwhile, the photovoltaic (PV) industry has experienced explosive growth in the last decade due to supportive policies world widely and marked rising fossil fuel prices (Fig 1.1). The gap between retailed electricity price and PV-generated electricity price is closing fast. Although the industry is weathering a period of uncertainty in the last few months, the prospects for continued growth are good in a long run. In fact, 29.7GW of PV systems were connected to the grid in 2011, with the growth rate around 70% in 2011 where Europe countries, Italy and Germany in particular, contributed to 60% of global market growth, followed by the Asia-Pacific region, mainly China, Japan and Australia, then North-America in the third place as shown in Fig 1.2[1]. These new installations bring the world to an estimated 67.4GW of global PV capacity at the end of 2011. PV has been catapulted into the third most important renewable energy in terms of globally installed capacity after hydro and wind power. It's predicted by the International Energy Agency (IEA) that PV generation should rise from 70GW to 230GW till 2017, contributing 4.9% to renewable energy generation.

Global Cumulative Installed Capacity 2000-2011

	2000	2001	2002	2003	2004	2005	2006	2007	2008	2009	2010	2011
Europe	154	248	389	590	1297	2299	3285	5257	10554	16357	29777	51716
APAC	355	491	677	902	1718	1475	1797	2080	2643	3409	5116	7769
America	146	177	222	287	379	496	645	856	1206	1744	2820	5053
China	19	30	45	55	64	68	80	100	145	373	893	3093
MEA	0	0	0	0	0	0	0	0	0	21	205	336
ROW	751	807	887	964	993	1003	1108	1150	1226	1306	1209	1717

Figure 1-1 Evolution of global cumulative installed capacity 2000-2011. ROW, MEA and APAC stands for rest of the world, Middle East and Africa, and Asia Pacific respectively[2].

Global Annual Installation Share in 2011
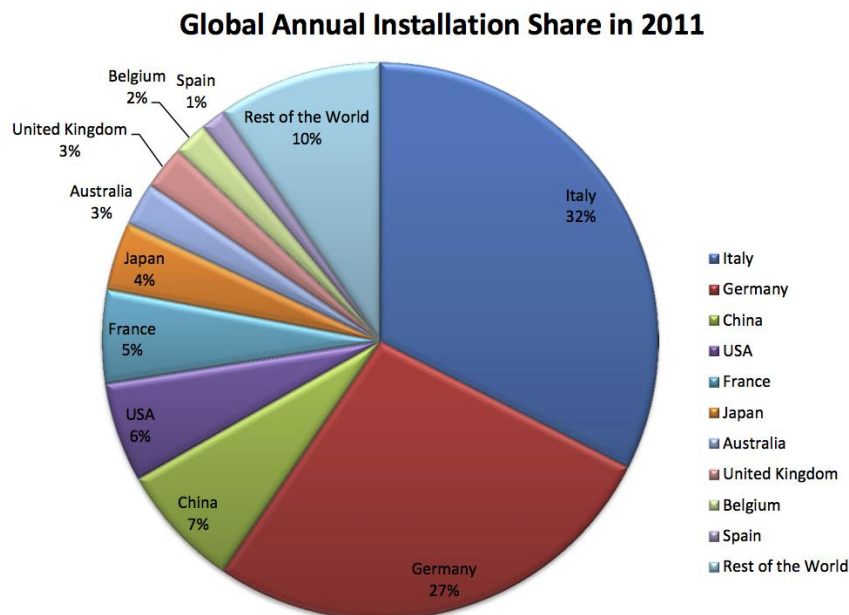
Figure 1-2 Global annual installation shares in 2011 estimated by European Photovoltaic Industry Association (EPIA) [1].

2

The mainstream of PV industry is crystalline silicon based solar cells, namely monocrystalline or multicrystalline solar cells, which is also known as the first generation solar cells. With the most mature technology and durable performance, they account for 80% to 90% market share (Fig 1.3). Monocrystalline silicon cells are the most efficient with a relatively high cost since thick high purity silicon wafers (around 200μm) are required and additional cutting loss are inevitable when cutting from ingots. Multicrystalline, or poly-silicon solar cells, have a little less efficiency around 15% to 18%. Both of them have been proved stable practically. Usually it's guaranteed to remain 80% of the nominal power output after 25 years operation by manufacturers. Intense effort has been put to reduce cost by optimizing process, develop novel methods. However, the achieved maximum efficiency of monocrystalline silicon cells in lab is 25%, close to theoretical value, there, the cost reduction potential seems limited.

Unlikely, thin film solar cells grow thin active layers on cheap substrate and emerge in the last decade. Typically, thin film solar cells have a thickness of less than 10μm, far less than crystalline cells, which make it really competitive from the material consumption consideration. On the other hand, thin film solar cells can be manufactured monolithically, which allows large area cell fabrication and continuous processing; it also lowers the material cost and reduces final module cost eventually. Easy manufacture process enables large throughout put possible. It has been reported that manufacture time can be reduced to less than 2.5 hours for thin film solar cells (CdTe by FirstSolar). Also, thin film solar cells can be deposited on flexible substrates which bring in promising opportunities in building integrated PV (BIPV) field. It's also worth mention that thin film solar cells are less affected from indirect irradiation than crystalline cells whose performance suffers from steep drops as the angle of solar incidence gets steeper.

2010 Cell Production by Technology (MW-%)

Thin film Si, 1,349, 5%

CIS/CIGS, 426, 2%

CdTe, 1,438 6%

Monocrystalline Si, 920, 4%

Multicrystalline Crystalline Si 19,768, 83%
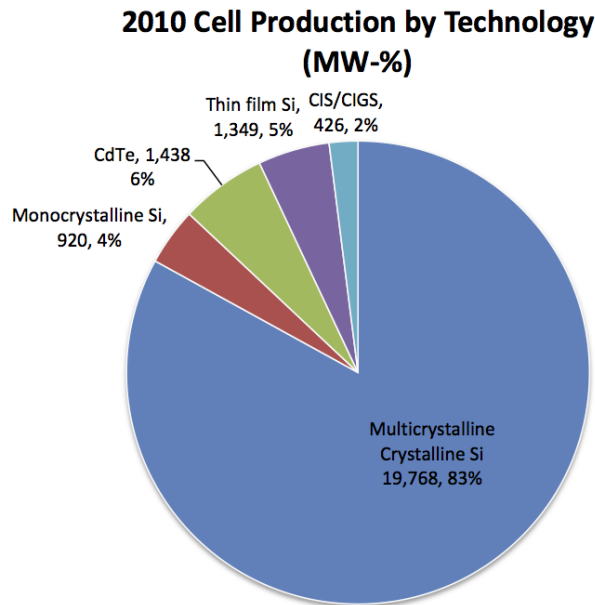
Figure 1-3 2010 solar cells production by technology[3].

1.2   Objective

The target of this thesis is to develop high quality amorphous silicon and mirco-crystalline silicon (μc-Si) by Plasma Enhanced Chemical Vapor Deposition (PECVD), both intrinsic and doped. PECVD is the most common tool to deposit device grade a-Si:H film. Compared to a-Si:H films, μc-Si has less defect density and doesn't have light-induced degradation problem. Furthermore, doped μc-Si has 3-4 orders of magnitudes higher conductivity than doped a-Si:H, however, the main limiting factors are very low deposition rate and large area uniformity. In this thesis, high conductive μc-Si films and high deposition rate have been developed by PECVD and modified Inductively Coupled Plasma Chemical Vapor Deposition (ICP-CVD). Moreover, silicon-germanium compound will be developed by modified ICP-CVD. a-SiGe:H has tunable energy bandgap which would be applied on tandem solar cells. Developed films have been characterized by conductivity, Raman sepctra, cross-section TEM, XRD etc. And heterojunction solar cells will be fabricated by these films, dark and illuminated IV have been analyzed, and external quantum efficiency has been measured. The thesis is organized as follows:

Chapter 1 intends to provide an overview of thin film solar cells;

Chapter 2 introduces existing thin film solar cells and common deposition tools, followed by growth mechanism of a-Si:H and μc-Si:H by PECVD;

Chapter 3 presents experiment results of deposition a-Si:H and μc-Si films by PECVD. Intrinsic a-Si:H was first deposited, characterized by Raman, then doping gases were introduced to form doped a-Si:H films, characterized by conductivity as a function of deposition conditions such as doping gas ratio, pressure, power etc. Moreover, doped μc-Si films were developed and characterized with emphasis on p-type μc-Si development;

Chapter 4 describes experiment results of μc-Si deposition by modified rf-ICP-CVD with Raman, XRD, and conductivity characterization;

Chapter 5 presents the a-SiGe:H films by modified rf-ICP-CVD and characterized by Raman, corss-section TEM and EDS;

Chapter 6 shows the heterojunction fabricated by these films, with EQE and I-V characterization;

Chapter 7 summarizes the work.

Chapter 2

Literature Review

2.1 Existing thin film solar cells

Thin film solar cells have grew vigorously from a paltry 68MW in 2004 to 2GW in 2009, once commanded 17% of the PV market in 2009[3]. The installed capacity increased to 3.7GW, occupied 11% market share in 2011 although crystalline silicon PV prices dropped by over 40% and initiated the virulent price war in PV industry. Generally, there are three leading thin film materials used in the manufacture of solar cells, amorphous silicon (a-Si), cadmium telluride (CdTe), and copper indium gallium diselenide (CIGS).

2.1.1 a-Si:H thin film solar cells

Amorphous silicon (a-Si:H) account for around 5% in PV market, have an acceptable efficiency from 7% to 10% at best. It has long been used in consumer electronics such as calculators and watches. Fig 2.1 illustrates the current p-i-n a-Si:H solar cells with soda-lime glass as superstrate through which light enters and passes to cell layers sequentially. Substrate configuration, the other structure of thin film solar cells, is opposite where light enters cell layers first rather than the base layer. The present of intrinsic layer is to improve cell's performance. A-Si:H has extremely low minority carrier diffusion lengths ($\sim$ 0.1 to 0.3µm[4], which is over 200µm in crystalline silicon) due to its natural film quality, even worse after doping. The silicon dangling bonds act as recombination centers for carriers. And the Fermi-level can only be pushed half way towards the conduction and valence band edges, even with heavy doping. All these factors make it impossible to collect carriers efficiently. So the intrinsic layer is added to generate free carriers whereas doped layers are to set up electric field and sweep carriers to contacts.

Moreover, most a-Si solar cells adopt p-i-n structure instead of n-i-p structure. This is because the mobility of electrons in a-Si:H is roughly 1 or 2 of magnitude larger than that of holes, leading to higher collection rate of electrons moving from n- to p-type contact than holes moving from p- to n-type contact, the majority of the charge carriers crossing the junction would be electrons by placing p layer close to strong light intensity region. One thick layer of TCO (1µm) is deposited on glass to insure good conductivity (typical sheet resistance 10Ω/sq[5]), also it's textured to trap light. Then active layers are deposited by chemical vapor deposition. The doped layers are quite thin, around 10-20nm, only to set up the electric field. As the absorber layer, intrinsic layer should be thick enough

(1μm) to maximize light absorption, however, it suffers from 15% to 35% efficiency degradation when first exposed to sunlight, called Staebler-Wronski effect. Due to this main constraint, a-Si:H PV technology has lost ground from ~39% PV share in 1988 down to ~10% in 1997 and less than 5% in 2010[3][6]. Some companies are working to reduce a-Si:H layer thickness (more stable) by employing excellent light trapping schemes. Another restriction is the spatially nonuniform of a-Si:H layer and the transparent conductive oxide (TCO) layer on a large substrate (>1m^2).

Glass (soda lime)

Front TCO (SnO2 or ZnO:Al)

P+ (a-SiC or μc-Si:H)

i (a-Si:H)

N+ (a-Si:H or μc-Si:H)

Rear TCO (ZnO:Al)

Rear contact (Ag)
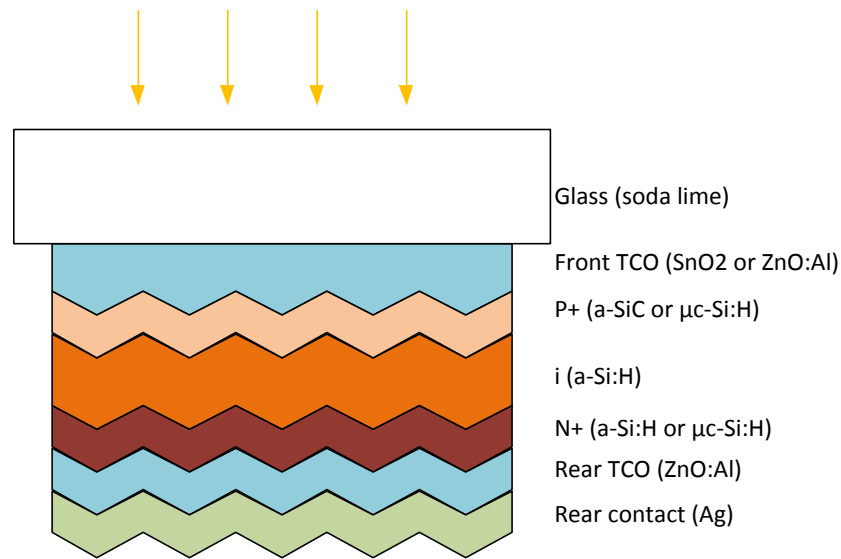
Figure 2-1 Schematic structure of current p-i-n a-Si:H solar cells in superstrate structure**[5]**.

2.1.2 Micromorph

Whereas the new concept of micromorph solar cells has combined a-Si:H with microcrystalline silicon layers, in a top and bottom structure shown in Fig 2.2. Due to different band gaps between a-Si (1.7eV) and c-Si (1.1eV), spectrum absorption is broadened and enhanced, moreover, these two materials can be manufactured in the same technology, usually PECVD or VHFCVD. Because microcrystalline silicon is indirect band gap material, so the thickness of bottom cells is designed much thicker than top cell. In addition, one intermediate reflector layer can be inserted between top and bottom cells to improve light confinement, which is a heated topic nowadays and could further reduce the a-Si:H thickness achieving better stability. So far, the reported highest initial cell efficiency was 15% (1cm^2) by Kenji Yamanoto et al. in 2005[7]. The best stabilized efficiency was reported 11.9% in 2010 from a joint research between Oerlikon Solar Lab and Corning

Incorporated[8], and this improvement is remarkable for commercialization. The output in 2010 is 120 MW.

Sunlight

Class
TCO
a-Si p-layer
a-Si i-layer
a-Si n-layer
μc-Si p-layer
μc-Si i-layer
μc-Si n-layer
ZnO
Ag

a-Si top cell

μc-Si bottom cell
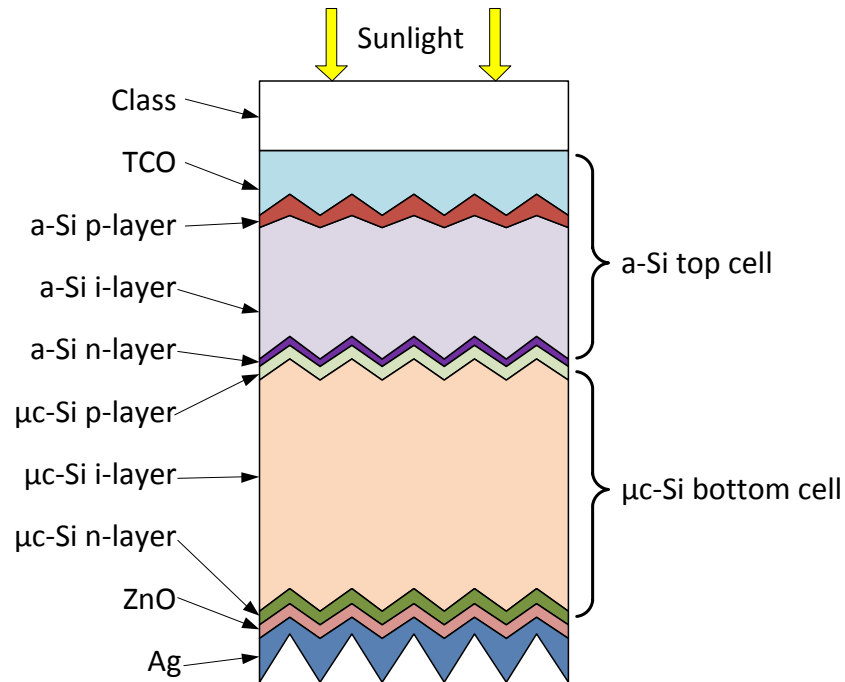
Figure 2-2 Structure of micromorph solar cells.

2.1.3 Tripe junction silicon solar cells

Similar to micromorph stacked structure, triple junction silicon solar cells have the structure of p- a-Si:H-n/ p- a-SiGe:H -n/ p-a-SiGe:H –n, manufactured by United Solar shown in Fig 2.3. With different germanium concentration, the band gap of a-SiGe:H material can be easily engineered, to modify solar spectrum absorption. Although it has multiple layers, this type of tripe junction solar cell could be very thin even below 0.5μm and the stable efficiency is around 8.5%. Flexible steel is used as substrate, which allows roll-to-roll fabrication and produces 180 MW/year in United Solar[9]. In the p-i-n structure, p and n layer do not have to be the same material as i-layer. They form p-n junction across the i-layer. More importantly, the inter-layer (i.e. n3, p2, n2, p1) are supposed to form ohmic contact by tunneling effect. Therefore, those layers are normally very thin and heavily doped to form tunnel junctions. To achieve more competitive triple-junction cells, Uni-Solar is now moving to use nc-Si:H as bottom cell material. (nc-Si, micro-Si and μc-Si are the same material) The high wavelength response and low light-induced degradation makes nc-Si:H preferable not only in double junction tandem cells but also triple-junction cells. With the structure of a-Si:H/nc-Si:H/nc-Si:H, Uni-

Solar has reported the world record tandem cell stabilized efficiency of 12.4% in 2011[10]. Although uniformity of large area deposition is challenge of VHF-PECVD method, it is still considered to be the most promising technique for high rate nc-Si:H deposition.
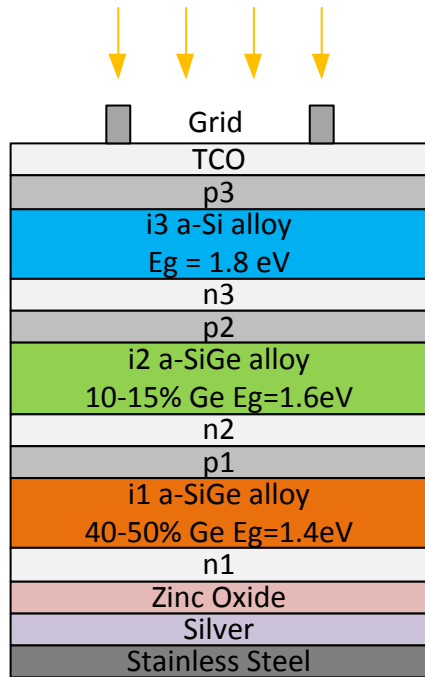
Figure 2-3 Schematic of a-Si:H/a-SiGe:H/a-SiGe:H tandem solar cell[**9**].

2.1.4 Polycrystalline silicon solar cells

Diffident from these cells based on amorphous silicon, polycrystalline silicon thin film cells is actually crystalline silicon with a grain size between 0.1μm and 1mm. The thickness of polycrystalline silicon cells is typically around 3μm. Unlike most a-Si based thin film, poly-Si doesn't have stability and reliability issues. With relatively large grain size, poly-Si has superior carrier lifetime and carrier mobility. Mostly, they are deposited by Aluminum Induced Crystallization (AIC) and Solid Phase Crystallization (CSG). The typical poly-Si cell structure is quite simple as shown in Fig 2.4. The TCO is eliminated since poly-Si has sufficient conductance for ohmic contact formation together with metal. This would not only lower the process cost but also further improve module durability. While due to large thermal budget and low through output, it moves slowly in industry.
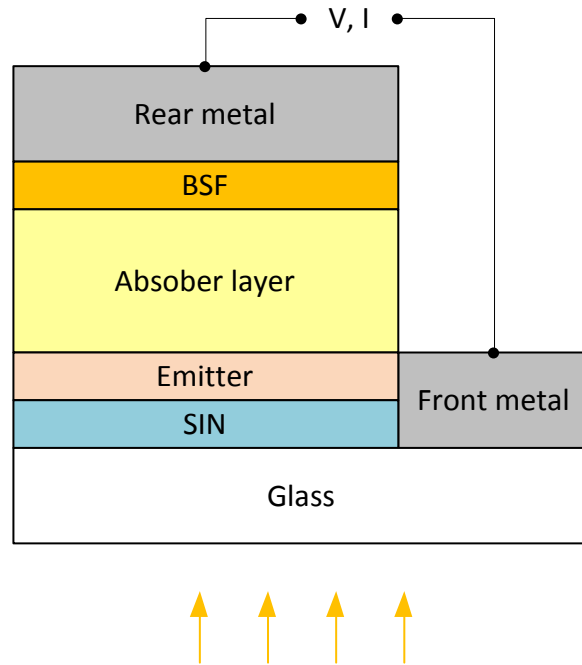
Figure 2-4 Schematic of poly-Si thin film solar cell**[11]**.

2.1.5 CdTe solar cells

Similarly, another polycrystalline material -- CdTe (most from First Solar), with efficiency ranges between 9% and 14%, has made up nearly half of total thin film production due to lowest Wp (Watt-peak) production cost as a result of easy manufacture. CdTe is the absorber in CdTe cell, a direct band gap material with 1.44eV at 300K, optical for terrestrial PV applications. Almost 92% of useful sunlight could be absorbed within the first micrometer. To achieve the same value, crystalline silicon would be as thick as 200μm. As a result of super absorption property of CdTe, most carriers are generated close to junction and are easy to collect. CdTe has less recombination in grain boundaries and no severe impact of lattice mismatch which gives it excellent performance. Together with CdS, a wide band gap material, the heterojunction is formed. Both of them are naturally doped, avoiding additional doping process in deposition. Fig 2.5 demonstrates the schematic of CdTe cells with superstrate structure since superstrate configuration generally produces higher efficiency than substrates in CdTe solar cells.

- Front glass is usually soda lime glass, based on an overall consideration of transparency, transition temperature and price. Additionally, it is expected to absorb the harmful high energy light for EVA. It would be replaced by polymer in the case of flexible cells.

- Front contact is also supposed to be transparent. Nowadays, TCO (Transparent Conductive Oxide) is widely used such as ITO (Indium Tin Oxide), SnO_2 and ZnO. TCO is very important for monolithic manufacturing.

- Semiconductor part consists of two layers: n-CdS (~ 100nm) and p-CdTe (~ 10μm) which form a heterojunction.

- Back contact is composed of a thin metal layer, which is a bottleneck for CdTe thin film solar cells because of large energy barrier between p-CdTe and aluminum or copper contacts. It's usually deposited at the end of the cell to have a better control, which makes most CdTe cells superstrate configuration.

- EVA layer provides good adhesion to glass. Hence, the laminated structure can provide "encapsulation" and then help the module to resist moisture penetration. Also the EVA could provide structural support, electrical and physical isolation for the solar cells and thermal conduction path to glass which help cooling the solar cells. This layer is ignored for flexible cells

- Back glass (back cover) together with the top glass provide the mechanical strength for the module. Ignored for flexible cells.

To date, the highest efficiency record of CdTe cell on glass was 17.3% set by First Solar with commercial-scale manufacturing equipment and materials in 2011[12]. And they have also improved the CdTe module efficiency to 14.4% in the same year. The manufacturing time for CdTe modles is as short as within 2.5 hours from a bare substrate to a module. Recently, the flexible CdTe cells achieved 13.8% efficiency using thin polyimide developed by Dupont in superstrate[13], 7.3% in substrate[14], and 7.8% with metallic foils in substrate[15]. However, Cd is toxic and needs to be recycled. Te is rare, availability problem of Te could arise in the long run.
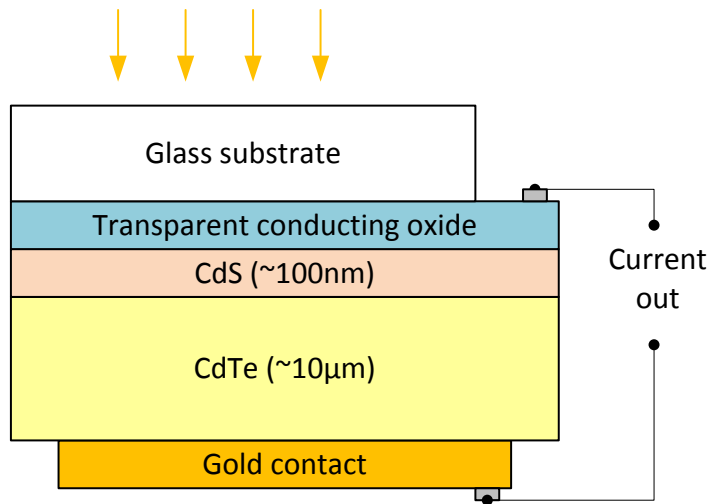
Figure 2-5 Schematic of CdTe thin film solar cell

2.1.6 CIGS solar cells

Before the recent breakthrough of CdTe cells, CIGS used to have the higher efficiencies than any other thin film material at 12 to 15.5%. Fig 2.6 shows the typical substrate structure of CIGS cells. Like most other thin film technologies, TCO layer acts as front contact. Like CdTe cell, a thin CdS layer is deposited to form heterojunction, replaceable with intrinsic ZnO. CIGS layer is actually a complex system consisting of five elements: copper, indium, gallium, selenium and sulfur, and is treated as polycrystalline material. The thin molybdenum layer, between CIGS and substrate, acts as a buffer layer to prevent shunting. The standard substrate is soda-lime glass where sodium can diffuse into cell and benefit cell efficiency. To date, the maximum cell efficiency on glass substrate was 19.9% by NREL in 2008[16], module efficacy was 14.8% in 2012 by Stion[17]. Recently, there was a big breakthrough of flexible CIGS cells and modules. The maximum cell efficiency was 18.7% or 17.7% on polymer or metal foil substrate achieved in 2011. And the flexible module efficiency was claimed 15.5% in 2012 by MiaSole[18], noting it's an aperture-area efficiency. The previous record was 13.4% by SoloPower in 2011. This achievement may close the gap between CIGS glass modules and flexible modules. The high efficiency, lightweight, no-mounting requirement makes it an excellent candidate for building integrated photovoltaic project (BIPV). While large area production is hard to achieve, the flexible CIGS module at record efficiency is 1.68 m^2 from MiaSole[19].
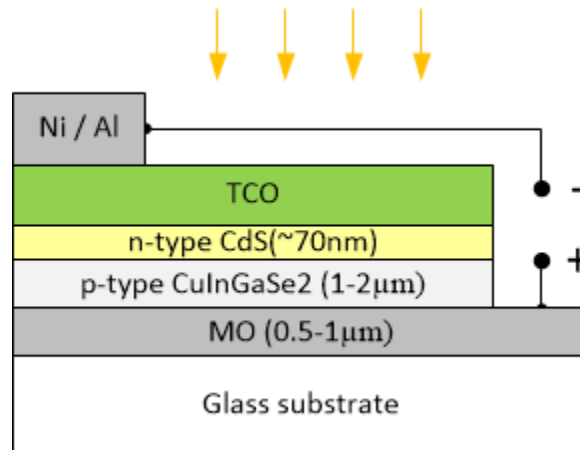
Figure 2-6 Schematic of CIGS thin film solar cell[20]

2.1.7　Monolithically interconnection in thin film solar cells

It's well known that contacts of crystalline silicon are done by screen printing of aluminum and silver paste on single cell, followed by up to 850°C co-firing. However, it increases breakage possibility of thin wafers and silver price is escalating. In the case of thin film cells, some can be manufactured in a similar way as a series of individual standard cells connected together, whereas the other method monolithic series interconnection is more favorable where a series of cells are monolithically interconnected during the film deposition process by patterning three sets of scribes, called P1, P2 and P3 for short . In typical industrial production, these scribes in Si and CdTe modules are cut by lasers with different wavelengths. While only P1 in CIGS modules is performed by a laser, P2 and P3 are done in a mechanical way with needles due to weak adhere between layers[21]. Compare to mechanical method, laser is able to perform very precise and thin scribes with well-defined edges, as a result, the dead area zone of the modules is minimized. Therefore, it has been the preferred technology for thin-film scribing since the beginning of thin film production over 10 years ago although it's a little expensive than mechanical ways.

Fig 2.7 demonstrates the formation of monolithic integration of a-Si:H superstrate structure. P1 is first cut from glass side to define cell regions which are usually around 1cm wide with the same length of module. P2 is cut in a way to connect the front of conductive active layer to the back of adjacent cell. And P3 is to isolate cells' metallic back contacts. Due to the precision of laser, generally the width of each scribe is 50 -150μm, similar to the horizontal distance between them, adding up to 500μm long interconnect region in typical, which actually does not contribute to photocurrent. However, the distance between scribes can't be infinitely small in order to get good isolation and a low sheet series

13

resistance. Monolithic interconnection makes use of the sequential nature of thin-film processing and arranges cells to match desired output. However, the drawback is up to 15-25% parasitic loss related with the TCO layer.
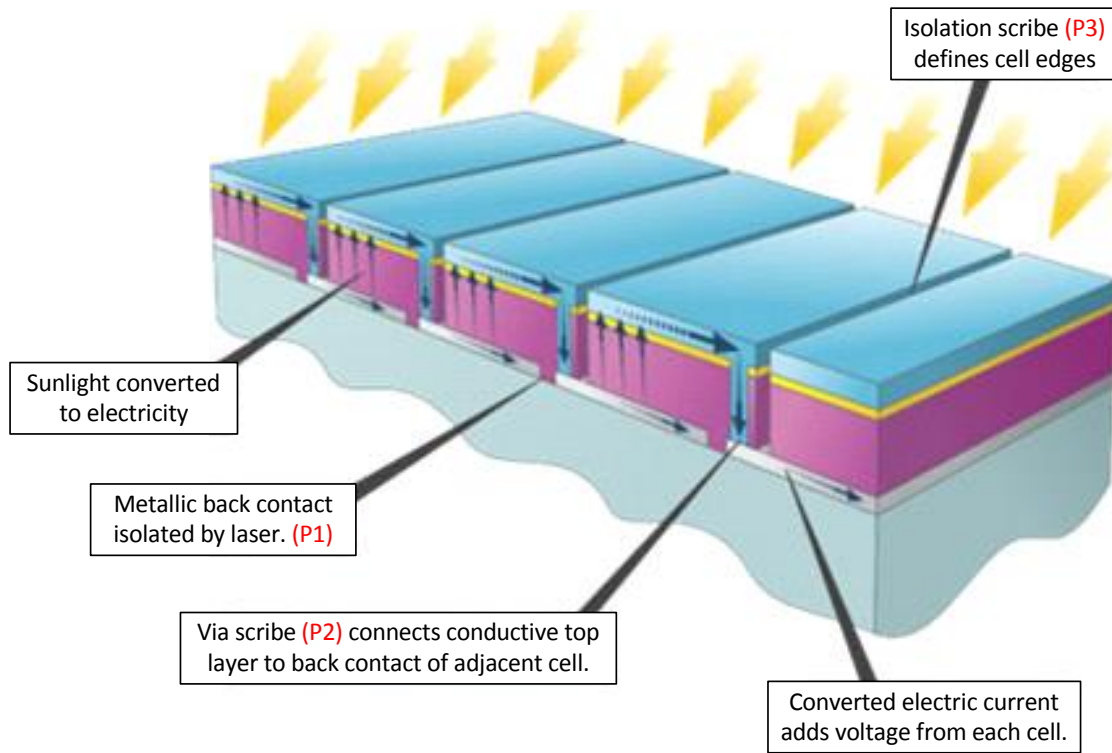
Figure 2-7 Formation of monolithic integration of a-Si:H cell with P1,P2 and P3 are scribes[22].

2.2 Methods for thin film deposition

This section will introduce several widely used deposition tools for silicon-based thin film solar cells both in industry and in research laboratory.

2.2.1 Radio Frequency Plasma Enhanced Chemical Vapour Deposition (rf-PECVD)

PECVD is the most common deposition tool for "device quality" a-Si:H, it has several configurations such as bath-type, cluster tool, in-line etc. Fig 2.8 shows a common parallel plate reactor. The capacitive discharge is excited between the two cylindrical conductive electrodes by applying radio-frequency (rf) signal. Gases get dissociated by collisions and become a mixture of radicals, ions, neutral atoms, molecules, and other highly excited species. Due to the high mobility of electrons, the gas mixture shows positively charged, and a potential drop zone, called sheath, is formed between

14

plasma and neighbouring objects. Radicals will be accelerated to the objects after diffusing to the edge of plasma, and start film growth.

One important feature of PECVD is that high quality film can be developed at low deposition temperature. It's because the fractional ionization used for deposition is quite small, around 10^{-4} in rf PECVD. As a result, electrons maintain very high energy, several electronvolts average energy, due to inefficient energy transfer between electrons and neutral atoms, which ensures sufficient dissociation of precursor molecules and the generation of large amount of free radicals by collisions even at low deposition temperature. Device quality a-Si:H is normally deposited by SiH_4 gas between 200 to 250ºC at a rate of 2-5Å/s, which gives a wide range of possible low cost substrates, such as glass, stainless steel, flexible plastic foils etc. Doping is attained by adding proper gases with source gas, usually diborone (B_2H_6) or pyrophoric trimethylboron (TMB) for p-type, phosphine (PH_3) for n type film. Moreover, some other gases can be introduced to modify band gap, such as germane (GeH_4) or methane (CH_4). By controlling different gases, it's possible to deposit multi-layer structures in a continuous process. And film deposited by PECVD has good adhesion and uniformity. In fact, the fast development of liquid crystal displays (LCDs) has upgraded PECVD with large-scale, high-throughput capacity, giving over 10 MWp/year output of single-junction a-Si:H PV modules on 1.4 m^2 glass wafers[23].
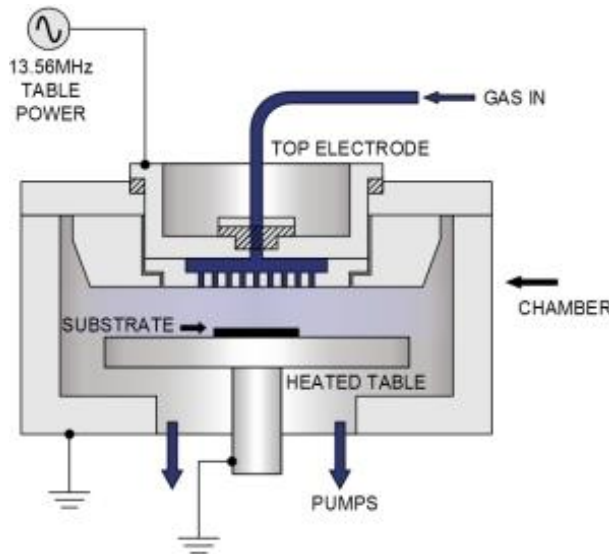
Figure 2-8 Schematic graph of rf-PECVD**[24]**.

2.2.2 Inductively Coupled Radio Frequency Plasma Chemical Vapor Deposition (ICP-CVD)

Compared to conventional PECVD, ICP-CVD has much higher plasma density due to inductive discharge. Fig 2.9 shows one typical structure of ICP-CVD. Powered by a high-frequency signal, usually 13.56 MHz radio frequency, the inductive coil outside dielectric walls will generate a magnetic potential in the chamber, in which radicals will be accelerated in the plasma rather than just at the sheath edge. It should be noted that the induced current is opposite to the coil current, parallel to the bottom electrode where wafers sit on, and radicals will diffuse down to the wafer instead of drift, to minimize energetic ion bombardment to wafer surface, which is essential for high quality film. Furthermore, there is normally no bottom RF power applied to ensure low plasma-induced damage and stress level. When excited by inductive discharge, the deposition pressure of ICP can be quite low, usually well below 100mTorr, in contrast to other plasma processes where pressure has to be kept above certain level to maintain impedance in order to resistively heat up electron.

Due to high plasma density, ICP can achieve high deposition rate without comprising film quality by changing ICP power and gas flow rate. It has been utilized to deposit silicon oxide, nitride, carbon nanotube. It gives very good step coverage even at quite low temperature whereas typically high temperature as 300ºC is required to get good coverage in PECVD.
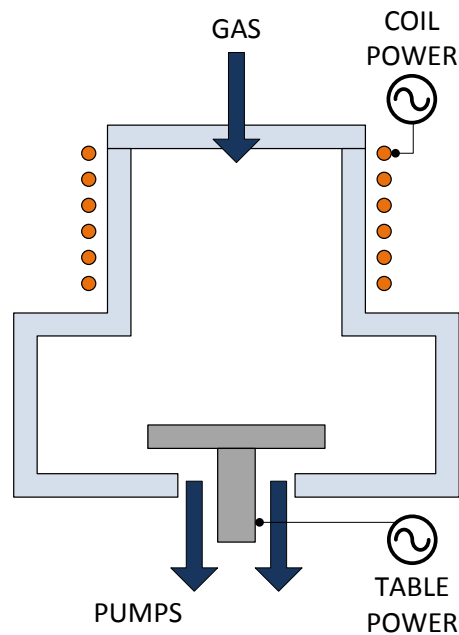
Figure 2-9 Schematic graph of ICP-CVD

2.2.3 Very High Frequency PECVD (VHF-PECVD)

In order to increase deposition rate, as high as 30-300 MHz excitation frequency has been applied on PECVD after the finding that very high frequency could accelerate ionization. The amorphous silicon deposition rate has been proved to be two to ten times higher compared rf-PECVD. It's because the shealth width is reduced at very high frequency circumstance and thus more RF power is coupled into plasma. Furthermore, the ion bombardment becomes softer while more intense, which is favorable for microcrystalline material formation. It's reported that microcrystalline films can be developed at the rate of 1-3nm/s [25]. Consequently, it prompts the development of micromorph cells, and some companies such as Inventux Technologies AG, Bosch Solar Energy G, Baoding Tianwei Solar are using such technique. The main drawback is hard to scale up to large area (in the range of 1 m^2) as a result of non-uniformly distributed voltage on electrodes. Recently, researchers in the Mitsubishi Heavy Industries has announced that the new design ladder shaped electrode could improve uniformity[26]. They have successfully deposited uniform amorphous silicon film on 1.4×1.1 m glass substrate, with a rate of 1.7nm/s.

2.2.4 Hot Wire Chemical Vapour Deposition (HW-CVD)

Compared to plasma-assisted process, HW-CVD usually gives better film quality due to the absence of plasma i.e. no plasma-induced surface damage. Some filaments are introduced into chamber instead of two parallel electrodes, which are usually made of tungsten or tantalum and will be heated up during deposition. Typically for a-Si:H deposition, silane is thermally decomposed with filaments heated around 1600ºC to 2000 ºC, deposited on substrate at 250 ºC -350 ºC, with an acceptable rate of 10Å/s[27]. μc-Si:H film has been developed with high deposition rate as well, while no satisfactory solar cells has been made with high rate yet. The main problems include overheating of deposited film, regular filament replacement, and non uniformity on large area.

2.3 Growth mechanism

2.3.1 Growth of a-Si:H in PECVD

Amorphous silicon has a irregular atomic structure and lacks of long repeatable structure. Not all silicon atoms are fully bonded with others, leaving some unpaired bonds, called "dangling bonds" which are mostly passivated by hydrogen atoms. The existence of regular short range order makes it possible to use energy band concept to analyze a-Si:H. Fig 2.10 shows the impact of the lack of cyrstallinity on the density of states. The dangling bonds introduce broadly distributed density of states throughout the energy range, which is supposed to be "forbidden band" in crystalline silicon.

Also, band edges have extended into forbidden band, named "band tail", compared to the sharp band edges in c-Si case. The stretched or compressed Si-Si bond can easily break and form new defects in the amorphous network, as high as 10^{21} defects per cm^3 in pure a-Si has been measured [28]. When H_2 is incorporated into deposition process, the concentration of defects can be reduced dramatically, to 10^{15} to 10^{16} cm^{-3}, by bonding dangling Si atoms with H_2 atoms [29]. Typical H_2 contents in the bulk is around 10 atomic % [30]. The most favorable bond for high quality of a-Si:H is single Si-H bond, called mono-hydride (Si:H) bonds [31].
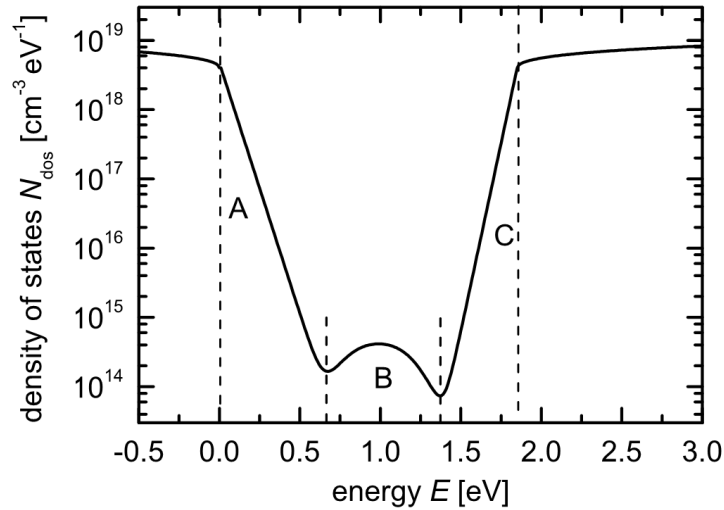
Figure 2-10 Density of states of a-Si:H calculated by a standard model**[31]**.

Generally, a-Si:H deposition in PECVD uses pure silane gas or diluted with helium or argon. In this thesis, pure silane is employed. Briefly speaking, gaseous silane get decomposed and react at active surface site, to produce solid silicon and gaseous byproduct H_2, as summarized by following equation suggested by Veprek [32]:

$$SiH_4 \xrightarrow{plasma} [SiH_n] \rightleftharpoons Si \downarrow + m[H] \tag{1}$$
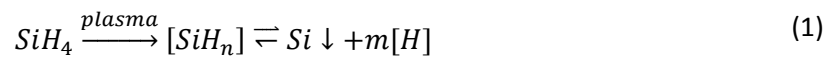
Fig 2.11 schematically illustrates the elementary mechanistic steps in a Si film growth process. It includes electron-impact induced excitation of SiH_4 to gas-phase silicon hydride radicals, gas-phase and surface reactions of these radicals, and desorption of byproducts from growing film, such as molecular hydrogen. The radical concentration is much less than stable molecules, and the dominant radical species is observed to be SiH_3[32], which has a fast reaction rate only with other radical species, while SiH and SiH_2 get consumed quickly due to rapid reaction with silane in the plasma. As

a result, SiH$_3$ takes the role to transport silicon to growth surfaces. SiH$_3$ has a quite low surface sticking coefficient around 0.04-0.08 on a hydrogenated silicon surface[33], along with SiH 0.94[34]and SiH$_2$ 0.15[29]respectively. Consequently, it's reasonable to assume, SiH and SiH$_2$, which can insert rapidly into Si-H bonds, would stick efficiently to a hydrogenated silicon surface, while SiH$_3$, which can't insert into Si-H bonds, would have to stick on a dangling bond site. It's reported that surface dangling bond density is approximately 10^{13}cm^{-2}, five to six orders of magnitude higher than bulk where the defect density is 10^7-10^{8}cm^{-2} per monolayer equivalent to 10^{15}-10^{16} cm^{-3}[35].

Also, it's proposed that SiH$_3$ can be inserted directly in a strained surface Si-Si bond[36]. SiH$_3$ is weakly absorbed by Si-H-Si bond on the surface which is called "physisorbed state", and diffuses quickly over the hydrogen passivated surface, and binds with dangling bond. A new reaction site is created when hydrogen is eliminated by a SiH$_3$ or another gas phase radical called Kisliuk mechanism. Also, weak Si-Si bond can be broken by mobile H, generating a dangling bond and a monohydride. In addition, the dangling bonds can be regenerated by electron and low energy ion impact under plasma conditions. When it comes to direct insertion of SiH$_3$ into a Si-Si strained bond, no dangling bonds are required for film growth. However, it's hard to explain continuous film growth due to limited number of strained bonds at the surface. Moreover, it's suspected that the smooth film surface (root mean square roughness < 5nm), is a result of effective diffusion of certain radicals across the surface which is not known yet.
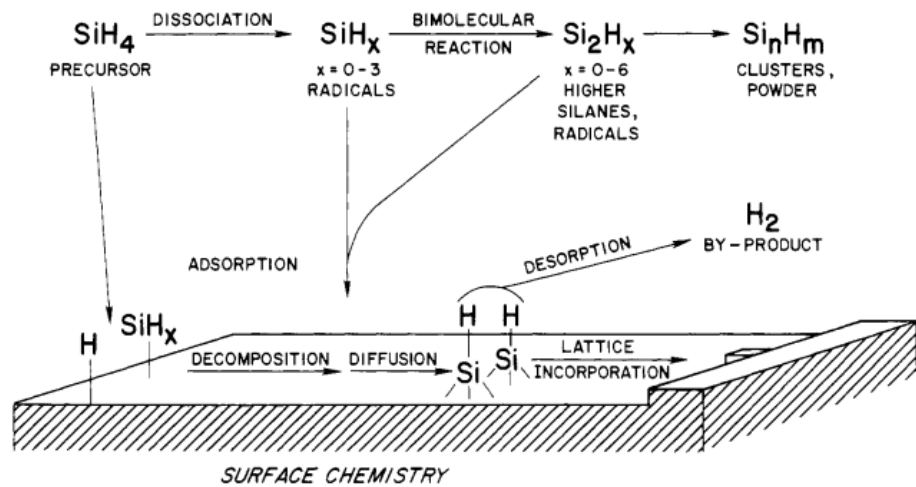
Figure 2-11 Schematic mechanism of Si film growth by a generalized CVD process, starting with SiH$_4$ precursor gas[32].

19

Amorphous Silicon could be doped by adding dopant gases as boron and phosphorus, which is relatively easy to achieve referring to continuous random network of a-Si:H compared to crystalline silicon with regular long range order. However, the doping efficiency is extremely low, around 10^{-2}-10^{-3} at room temperature[37], i.e. more than 90% dopants are inactivate, whereas in crystalline silicon almost all dopants are activated. The most widely accepted explaination for such doping phenomenon is the "autocompensation model" developed by R.A.Street[30]. Fig 2.12 schematically demonstrates the possible configuration of a phosphorous atom in an a-Si:H network. Dopants incorporate into a-Si:H network substitutionally. Most will form optimal threefold coordination which stands for the nondoping state and stay electrically inactive as Fig 2.12a, where 3 in $P_3 0$ indicates bonded to three neighboring atoms, 0 means neutral, no charge. Fig 2.12b depicts the effect doping state of phosphorus atom where positively charged P attracts negatively charged danging bond Si_3-, so-named "defect compensated donor", and Fig 2.12c is not favorable due to high stabilized energy. It should be emphasized that heavily doping creates extra defects in a-Si;H, the defect density is two or three orders of magnitude larger than intrinsic a-Si:H[4].

(a) $P_3^{\ 0}$ (b) $P_4^{\ +} + Si_3^{\ -}$ (c) $P_4^{\ 0}$

○ Si atom   ⬡ P atom   —— covalent bond   ▬ dangling bond
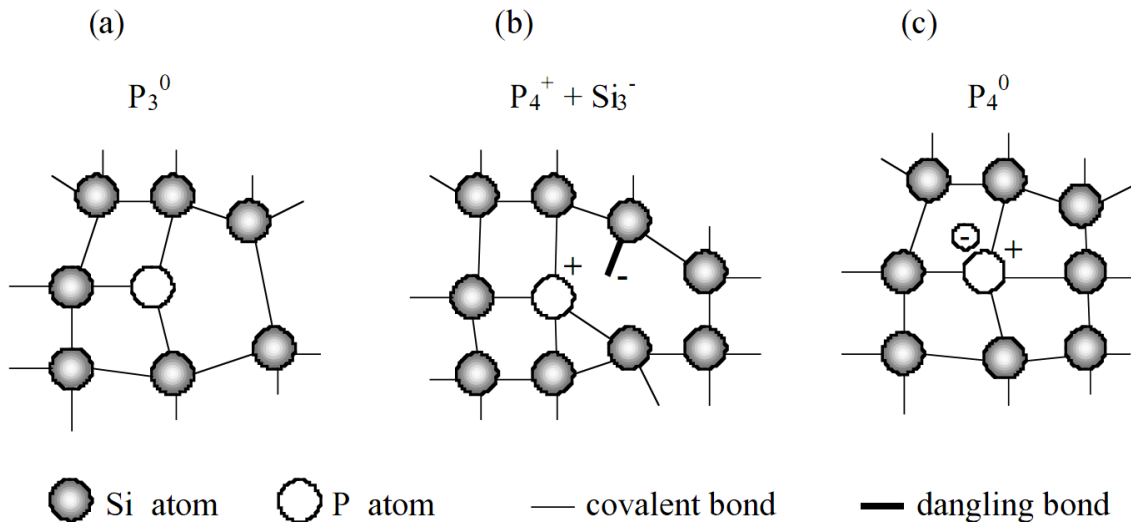
Figure 2-12 Possible configuration of a phosphorous atom in an a-Si:H network[4].

2.3.2 Growth of µc-Si:H in PECVD

Hydrogenated microcrystalline silicon (µc-Si:H) was first developed at 1968 by Veprek and Marecek[38]. The term "microcrystalline silicon (µc-Si:H)" or "nanocrystalline silicon (nc-Si:H)"

denotes films with nano-level crystalline grains in the amorphous network, usually deposited by PECVD at low temperature (< 400ºC) with highly H_2 diluted SiH_4 gas.

Fig 2.13 shows the absorption coefficient of a-Si, μc-Si, and c-Si in the range of photon energy from 0.5eV to 3.5eV where 85% of incident solar energy of AM 1.5 spectrum lies. μc-Si as an indirect-bandgap material, has lower absorption coefficient than a-Si at high energy range (>1.8eV), which means thick film (around 1-2μm) or better light trapping scheme is required for μc-Si to achieve same absorption with a-Si. And the energy absorption below bandgap, 1.7eV for a-Si and 1.1eV for μc-Si, is caused by defects, which would mostly act as recombination centers to annihilate light-generated e-h pairs. Apparently, μc-Si has lower defect density than a-Si, which makes it possible to have thick μc-si without dramatically increased recombination loss in μc-si layer.
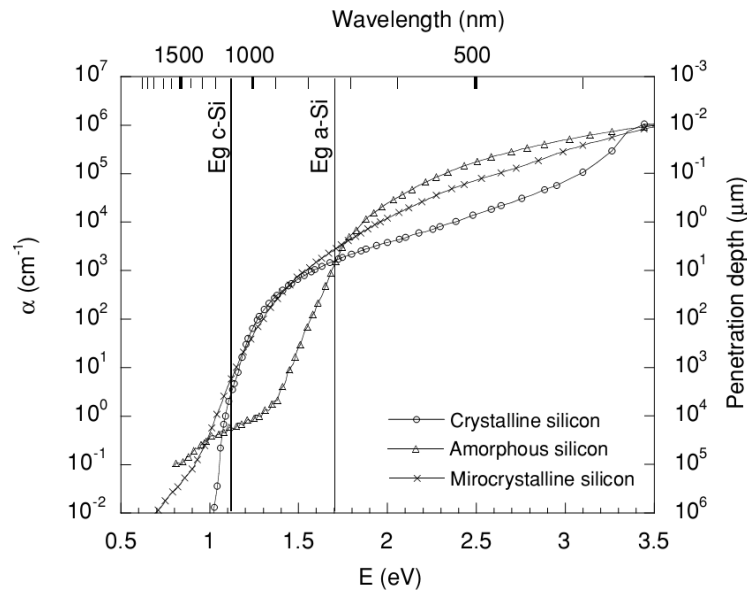
Figure 2-13 Optical absorption spectrum of μc-Si compared with a-Si:H and c-Si[4].

The high H_2 dilution in standard RF PECVD method limits the deposition rates to less than 5Å/s, which means hours will be taken for the deposition of 2μm thick film. Fig 2.14 shows a schematic diagram of μc-Si formation with high H_2 dilution[39]. Amorphous network is formed on the film-growing surface first and some Si-Si weak bonds are attacked by atomic H_2, removing a Si atom bonded more weakly to another Si (amorphous mode). New precursor will fill in that site and form a rigid and strong Si-Si bond (crystalline mode). High H_2 dilution is required to ensure etching sufficient which limits deposition rate simultaneously. It has been shown that by increasing the

deposition pressure (>1Torr) and forcing the plasma into the high pressure depletion regime (HPD) the growth rate is increased as high as 5Å/s. In this plasma regime, high hydrogen consumption and powder formation make the HPD process optimization significantly complex. By employing very high frequency (VHF), high quality microcrystalline films with very high deposition rates can be achieved. However, due to the formation of the standing waves on the electrode, it is extremely difficult to obtain uniform large-area (in the range of $1m^2$) μc-Si films.
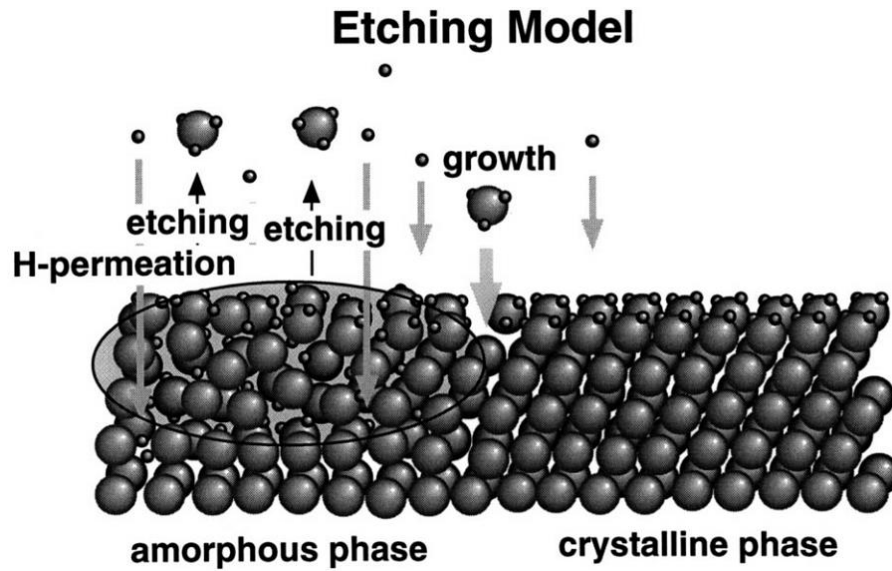
Figure 2-14 Etching model for μc-Si growth[39].

Chapter 3

PECVD deposition and characterization of a-Si:H and µc-Si

3.1 Intrinsic a-Si:H

The parallel plate PECVD with a vacuum loadlock by Trion Technology is employed. The a-Si:H film was deposited on Corning Eagle XG glass wafers with pure silane gas. Glass wafers were cleaned by standard RCA 1 process before going to chamber. The primary gases for a-Si:H is silane (SiH_4) or disilane (Si_2H_6), alone or mixed with hydrogen (H_2) or noble gases (He, Ar, Xe). In this thesis, a-Si:H films was developed from pure silane based on E.Fathi's work[40]. The deposition rate was 5Å/s when silane flow rate 20sccm. The film thickness was measured by Detek. Raman spectra were measured in the backscattering configuration using a Renishaw mico-Raman spectrometer with 488nm excitation laser line.

Fig 3.1 shows the Raman spectra of 300nm a-Si:H. The broad peak at 480cm^{-1} shows amorphous nature of the film. Although no H_2 gas was introduced, atomic hydrogen would be produced by electron and silane collision, which passivated dangling bonds in a-Si:H and improved film quality. By adding H_2 during a-Si:H growth, the film structure could change from amorphous to microcrystalline after surpassing a certain dilution ratio. The transition regime occurs in a hydrogen dilution range R= $[H_2]/[SiH_4] \approx$ 10-35[41, 42]. It's reported that defect density was minimized when deposited with pure SiH_4 gas and lower power. Moreover, an increased hydrogen content could lead to a larger instability of a-Si:H films[43]. The rf plasma power used in this work was 5 W, roughly 16 mW/cm^2, which was the minimum power of Trion rf PECVD. Because high RF power would induce high dissociation rate at the expense of film quality due to enhanced ion bombardment damage by rapidly accelerated ions, the film stress would become more compressive and impair film reliability. In comparison, high pressure at constant RF power leads to reduced ion bombardment due to the increase of collisions within plasma and increased deposition rate as well. It should be mentioned that high pressure could induce gas-phase polymerization reactions that causes powder formation, thus, the pressure range is restricted by the onset of powder formation, usually 0.01-1Torr is regarded as medium pressure range, and 1 to 10mTorr as low pressure range. Moreover, low pressure is preferable in order to conserve SiH_3 radicals till it encounters the growth surface. So the employed pressure was 200mTorr considering both film quality and deposition rate. The temperature was kept at 180˚C. The normal deposition temperature of PECVD is around 100-400°C in which range free

electron can gain sufficient kinetic energy by collision to activate excitation, ionization and dissociation with low gas temperature [44].
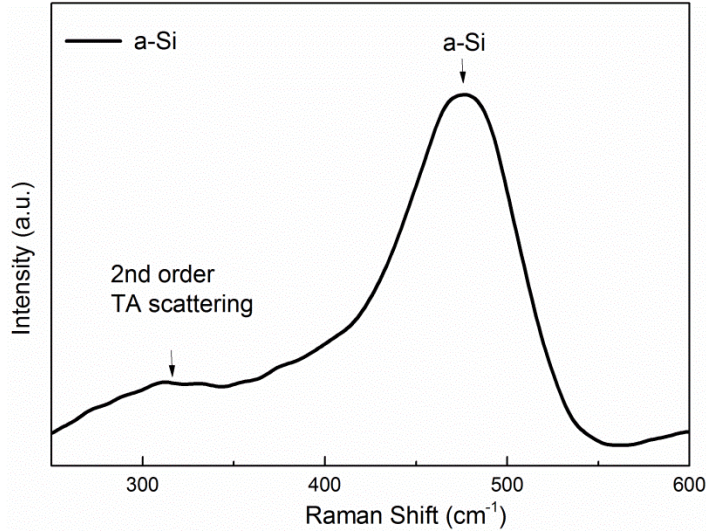
Figure 3-1 Raman spectra of a-Si:H.

3.2 Doped a-Si:H

In this experiment, phosphine gas, diluted with 99% H_2, was introduced into a-Si:H plasma deposition process for n-type film. For conductivity measurement, 18mm long and 1mm apart coplanar aluminum contacts were sputtered through a shadow mask by Intevac DC sputtering system. The I-V characteristics curve was measured by Agilent combined with a dark box work station. The conductivity was then calculated from the slope of I-V curve. And the film thickness was derived from transmission spectrum with the aid of a well-developed method [45].

It should be noted that a well-established chamber condition is required for good quality films and repeatability. During deposition, chamber interior was coated with films, also, particles formation were undergoing which has been studied by W.H.M.Lodders[46]. Small particles grew up to 2nm in the first few microsenconds once plasma starts, coagulated to 10-200nm after its density reached a critical value about 10^{10}-10^{11} cm^{-3}, and continued to grow till saturation. Some particles after reaching a certain weight would be flushed out of plasma, however, if the particles got too big, plasma would fluctuate. The existence of particles will pose effect on film quality and device reliability. Thus, after each deposition, the cleaning gas CF_4 diluted with O_2 was introduced into chamber and formed a plasma cleaning gas, which contacted interior surfaces of chambers and etched away deposited films

which were converted into gaseous forms and carry away. Such process is known as "in situ dry clean"[47]. The cleaning rate was determined by etching a glass wafer coasted with known thickness. Some residual reaction products by dry etching would adhere to interior surfaces of chamber, and may be absorbed by following deposition process, e.g. Fluorine would form particles when contacted by the reactive gases used to make oxide layer in PECVD [48]. In order to avoid the potentially undesirable by-products of cleaning, a subsequent layer such as a-Si:H, SiO_2 etc. was used to coat the chamber surfaces, from several hundred nanometer up to 2μm[49] thickness and 300nm was used in this thesis. Also, purgation by inert gases was carried out between cleaning and deposition to evacuate residue particles[50]. High pressure and high flow rate inert gas flow was on for one to three minutes and off for same time as a cycle, repeated for several times. After several deposition, visible particle formation and film peeling off have be observed, indicating "wet-cleaning" is required which needs to open the chamber and wipe the surfaces down with appropriate cleaning solvents[47], isopropanol (IPA) was used here. Strangely, it seemed the adherence of chamber walls was too weak to attach films and lots of large pieces of films started to drop off soon after starting a-Si:H passivation, shown in Fig 3.2. The plasma was stopped and another wet-cleaning was performed. H_2 plasma was applied before a-Si:H passivation. It turned out H_2 plasma had effectively removed any residues on the wall and the following a-Si:H deposition went smoothly. The a-Si:H passivation layer after wet-cleaning was kept at 1μm to stabilize chamber and insure repeatable data according to our experiments.
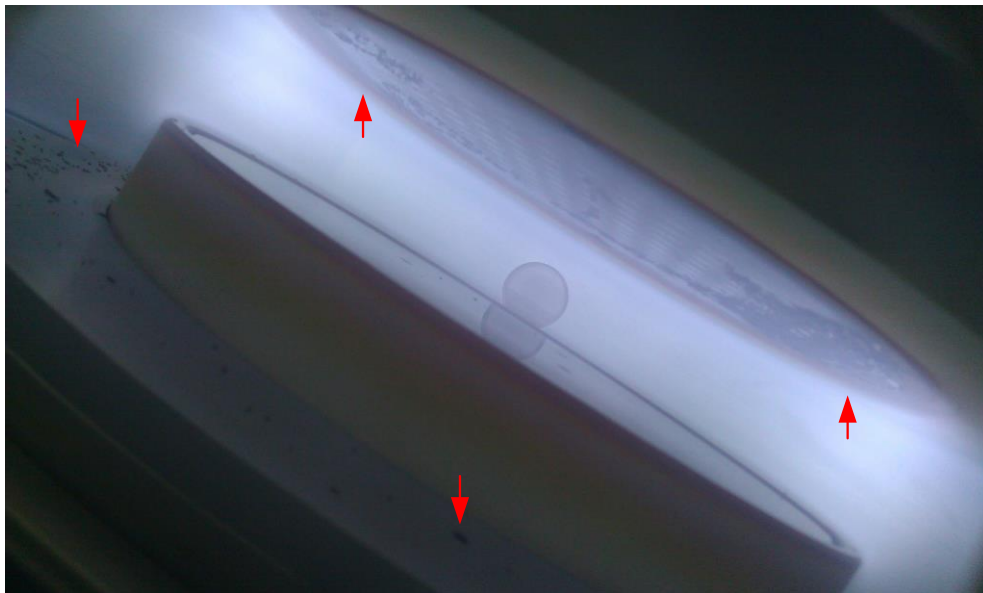
Figure 3-2 PECVD chamber with some peeling off after a-Si:H passivation.

Fig 3.3 shows the conductivity values as a function of PH_3-to-SiH_4 flow ratios. The silane flow rate was kept at 10 sccm, H_2 at 85 sccm with pressure 200 mTorr and power5 W. By increasing PH_3-to-SiH_4 ratio, the conductivity increased first then decreased. Compared to literature values [4], the conductivity was close to maximum values one could got at 180ºC. The deposition rate was 5nm/min, which could be a result of high H_2 dilution. In order to increase deposition rate, H_2 flow was eliminated and the SiH_4 flow was doubled from 10sccm to 20sccm, increasing the deposition rate to 8.8nm/min. The maximum conductivity without H_2 dilution was 1.15E-3 S/cm, which was in the range of highest conductivity at 180˚C by rf PECVD.
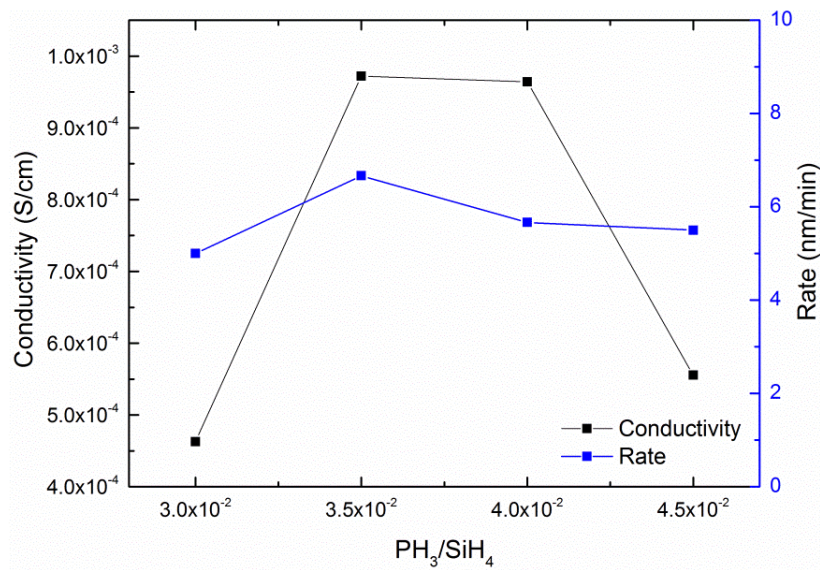
Figure 3-3 Conductivity and deposition rate of n type a-Si:H as a function of PH_3-to-SiH_4 ratio.

Fig 3.4 illustrates conductivity and deposition rate versus pressure. It's clear that the deposition rate increases with pressure as a result of more closely packed reactant gases where chances of collision, association and dissociation were increased. In contrary, the conductivity decreased with increased pressure which may be explained by reduced amount of positive ions P_4^+ due to collision, which are active dopant.
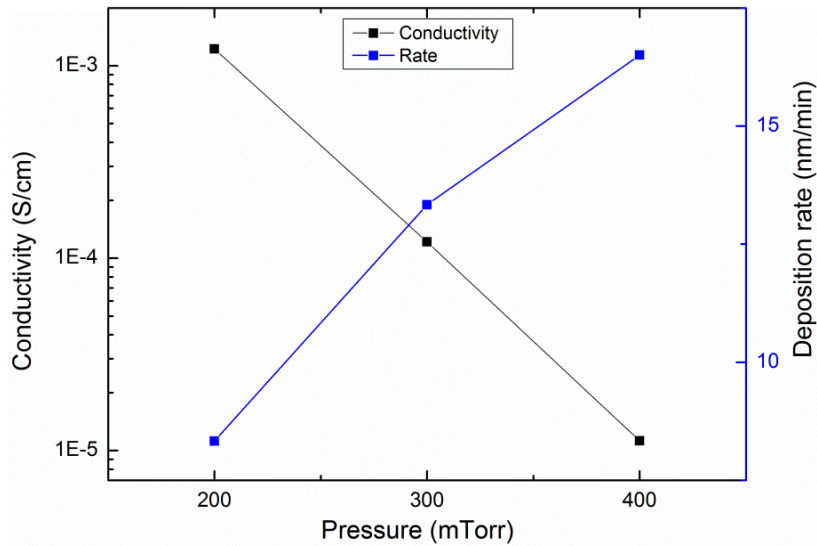
Figure 3-4 Effect of pressure on conductivity and deposition rate of n-type a-Si:H. The conductivity is shown in logarithmic scale.

Fig 3.5 presents the conductivity of n type a-Si:H as a function of deposition temperature. The silane flow rate was kept at 10 sccm, PH_3-to-SiH_4 =0.02 with pressure 200 mTorr and power 5W The conductivity increased to 7.78E-3 S/cm at 260℃ because the paramount –SiH_3 at low substrate temperature would develop into =SiH_2, and finally to dominate ≡SiH at high substrate temperature due to thermally enhanced H abstraction [41].
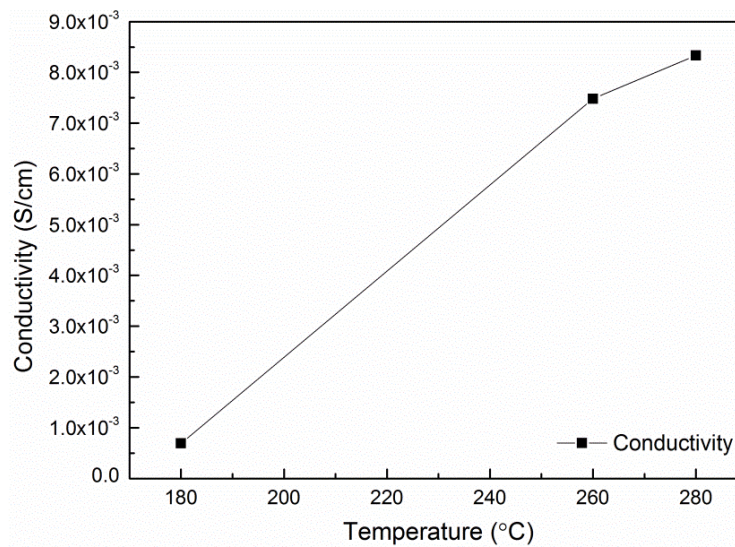
Figure 3-5 Effect of temperature on the conductivity of n-type a-Si:H.

P-type a-Si:H has lower conductivity than n-type film, the primary reason is that wider valence band tail prevents Fermi level farther away from the mobility edge, the other possible reason is that undoped a-Si is naturally slightly n-type due to the present of impurities such as oxygen, nitrogen. It has to be compensated first before showing p-type properties. Also, high power is required for diborone to get effective doping, which has been confirmed in p type µc-Si:H deposition in Chapter 4. However, this issue wasn't recognized when developing p type µc-Si:H films and the highest conductivity of p type µc-Si:H was 2.4E-4 S/cm, no further work has been done to achieve better conductivity.

3.3   n type µc-Si:H

Due to the localized crystallized parts, µc-Si:H experiences less light-induced degradation compared to its counterpart a-Si:H. And the unique structure enables easy doping and gives high conductivity, in the range of 10^1 S/cm and 10^{-2} for n-type and p-type film respectively. It has been studied that high H_2 dilution (~98-99%) would produce high crystalline percentage[42][51], since weak bonds are attacked and atomic structure is rebuilt. Fig 3.6 shows the crystallinity and dark conductivity of n-type µc-Si:H films as a function of PH_3-SiH_4 ratio deposited on glass subsrate[40]. The crystalline percentage reduced with increased amount of PH_3 gas since doping induced more defects and thus reducing crystallinity. The conductivity peaked when PH_3-to-SiH_4 ratio was around 0.75% with crystallnity around 40%. Similar PH_3-to-SiH_4 ratio has also been reported by[52]. Thus, n type µc-Si:H was developed in the similar range of PH_3-to-SiH_4 ratio. Deposition power was kept at 5W, pressure was 600mTorr, temperature was 180°C, and SiH_4 flow was 2sccm.

Fig 3.7 presents the Raman spectra of doped n-type µc-Si. It has been deconvoluted into characteristic spectrums. The crystalline silicon is dominated by a peak at 520 cm^{-1} originated from the transversal optical (TO) phonon, whereas this peak shifts to lower values as a result of finite grain size and internal stress, also the peak width increases[53][54].The broad peak at 471.8 cm^{-1} represents amorphous phase. Additionally, another peak is also observed at 501 cm^{-1} caused by the stacking faults in the crystalline phase, also referred to as wurtzite peak[55]. The crystallinity can be calculated by

$$X_c = \frac{I_{515} + I_{501}}{I_{515} + I_{501} + 0.80 I_{472}} \tag{2}$$

where I_X is the Raman intensity centered at indicated wave number, 0.8 comes from the different Raman cross sections for crystalline and amorphous silicon [56]. So the crystallinity was around 64.6%.

Furthermore, large grain size could cause the crystallized peak red shift towards 520 cm^{-1}, and small grain size would cause blue shift towards 480 cm^{-1}, so the average grain size (d) can be estimated by [57]:

$$d = 2\pi \sqrt{\frac{C}{\Delta\omega}} \tag{3}$$

where C is a constant, equals 2.24 nm^{2}cm^{-1} for silicon, $\Delta\omega$ the value of shift from nanocrystalline TO peak to crystalline TO peak. The estimated grain size was 4.1nm. And the conductivity was as high as 17 S/cm with a thickness 51 nm.
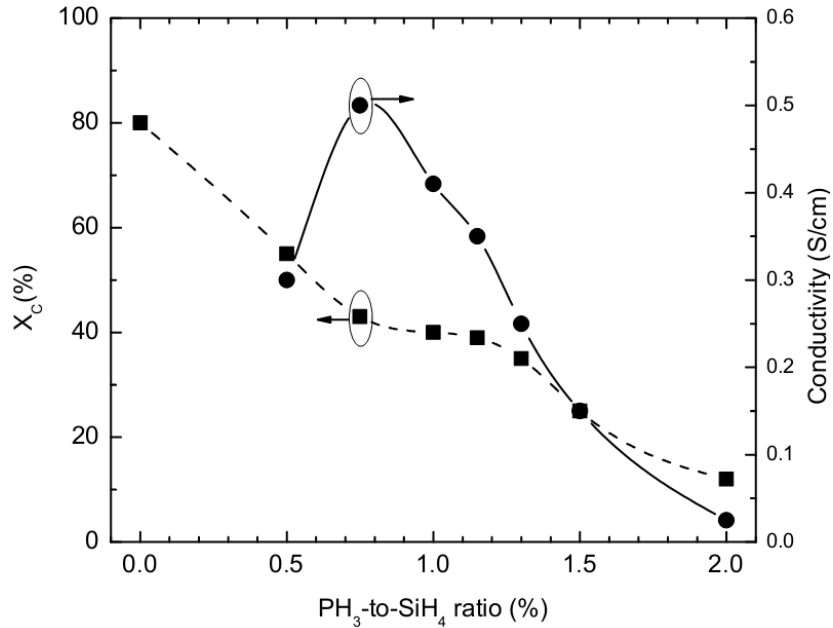
Figure 3-6 Crystallinity and conductivity of 40nm µc-Si:H as a function of PH$_3$/SiH$_4$ flow ratio[40].
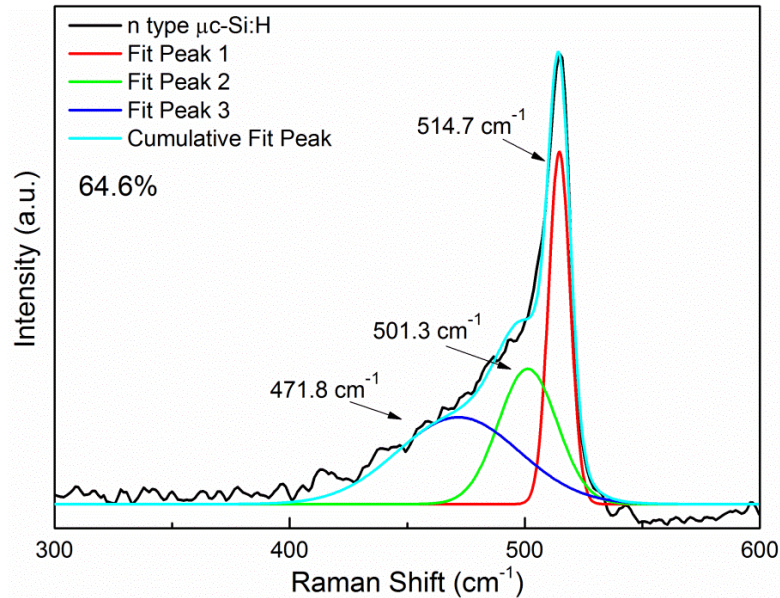
Figure 3-7 Raman of μc-Si:H deposited with PH$_3$-to-SiH$_4$ ratio 1%, H$_2$ dilution 99% at 180˚C.

3.4   p type μc-Si:H

More work has been done to optimize p-type uc-Si films, which could be used as front layer in p-i-n heterojunction solar cells with good conductivity and relatively lower defect density than p-type a-SiC:H window layers. Also, the built-in potential could be improved as a result of low activation energy of p-type μc-Si:H. It's well known that boron-doped uc-Si:H has one order lower conductivity than of phosphorous-doped silicon films. The challenges to get good conductive p-type uc-Si films come from several aspects:

- First, the undoped uc-Si:H film shows n-type naturally due to impurities such as oxygen and nitrogen, so compensation of n-type has to be made before "midgap" character [58].

- Second, boron has been reported to have a catalytic reaction with the hydrogen, enhance loss of surface hydrogen coverage, and disrupt the crystal growth [44].

- Third, the hydrogen atoms could passivate substitutionl B-Si bonds by forming the neutral B-H-Si complex [59].

- Forth, the film tends to become amorphous when boron concentration is in the range of 10^{20} cm^{-3} [60]. Furthermore, the boron doping efficiency is very low (10-20%) in PECVD [60].

30

In this thesis, pure silane SiH_4 and dibrone B_2H_4 which was diluted in H_2 to concentration 3%, were used. The deposition temperature was kept at 180ºC. All deposited p-type µc-Si:H films had a thickness around 50-80nm. Fig 3.8 shows the effect of H_2 on the conductivity and deposition rate. The SiH_4 flow rate was 2sccm, B_2H_6/H_2 0.6sccm and pressure 300mTorr. When H_2 flow rate increased from 200sccm to 400sccm, i.e. dilution ratio increased from 98.9% to 99.5%, the conductivity increased around 18%, and deposition rate decreased 17%. The abundant H_2 flow provided sufficient atomic hydrogen to reach fully surface coverage, also broke more weak bonds to increase crystallinity. As a result, conductivity increased at the expense of deposition rate.
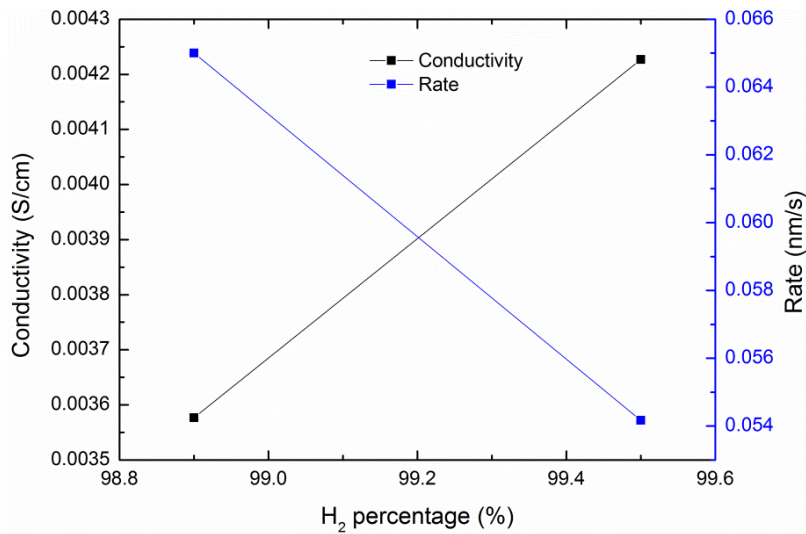
Figure 3-8 Conductivity and deposition rate of p-type µc-Si:H films as a function of H_2 dilution ratio.

Fig 3.9 depicts dark conductivity and deposition rate as a function of B_2H_6-to-SiH_4 ratio. The SiH_4 flow rate was kept constant at 2sccm with pressure 300mTorr and temperature 180˚C. The conductivities were in the range of 10^{-2} S/cm with B_2H_6-to-SiH_4 from 1% to 2.5%, and suddenly dropped to 1.1E-4 S/cm when B_2H_6-to-SiH_4 increased to 3%. The maximum conductivity in this series was 6.2E-2 S/cm when B_2H_6-to-SiH_4 ratio was 1.5%. When doping ratio was low, the amount of active dopants in film was low too, unable to get good conductivity since it was determined by carrier concentration and mobility. When the doping ratio exceeded a threshold value, the conductivity decreased although the carrier concentration was increasing, because heavily doping deteriorated film crystallinity and caused wider grain boundary barrier, thus enhanced the scattering effect in the grain boundary, which in turn reduced the carrier mobility and conductivity therein [60]. Another possible explanation was that the increased dopant concentration trapped larger amount of

31

atomic hydrogen to form neutral B-H-Si bonds complex, leading to insufficient flux density of atomic hydrogen to attack weak bonds, thus, the growth of microcrystalline was impaired, consequently the conductivity decreased. Moreover, it's found the sticking coefficient of film precursors SiH_3 on the film-growing surface increases with increasing boron-doping ratio [61].Furthermore, the deposition rate had a sharp increase when conductivity dropped rapidly, indicated possible reaction changes with more amorphous structure formation.
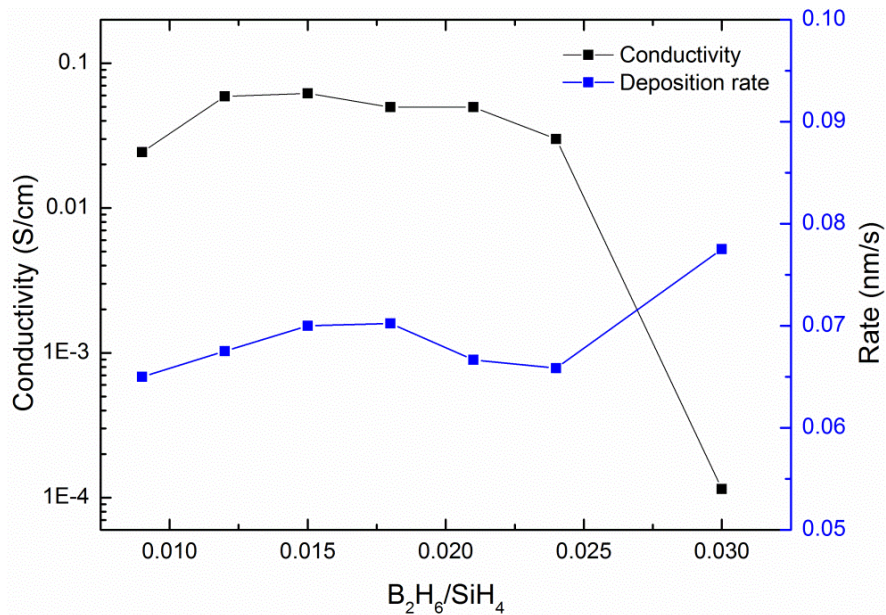
Figure 3-9 Conductivity and deposition rate of p-type μc-Si:H films as a function of B_2H_6-to-SiH_4 ratio. The conductivity is plotted on a logarithmic scale.

Fig 3.10 demonstrates the relation of chamber pressure on film conductivity and deposition rate. The SiH_4 was kept at 2sccm, and B_2H_6-to-SiH_4 was 0.009 with pressure 300mTorr and temperature 180°C. Sample series 1 and 2 had the same deposition parameters except series 2 were deposited after chamber being well cleaned and passivated while series 1 not. The deposition rates were very similar, while the conductivity improved, especially in the range of 300 and 400mTorr, conductivity increased nearly one to two orders of magnitude. The electronic properties of p type μc-Si:H has been greatly affected by chamber conditions, details could be found in doped a-Si part. Although values at 400mT varied a lot, both lines showed similar general trend of conductivity and deposition rate. Conductivity increased suddenly, peaked around 300-400mTorr and then decreased one or two orders of magnitude lower. The highest conductivity was 2.51E-2S/cm at 400mTorr after chamber conditions stabilized,

and was 4.23E-3S/cm at 300mTorr before cleaning. The changes may be explained by pressure-dependent H_2 incorporation into growing film. The density of atomic hydrogen (Hα) was proportionate to the generation rate of atomic hydrogen[62]:

$$[H_\alpha] \propto \sigma v_{th} N_e [H] \tag{4}$$

where σ is the dissociation cross-section of the collision, v_{th} the thermal velocity of electrons in plasma, N_e the density of energetic electrons responsible for the reaction, and $[H]$ the density of atomic hydrogen. The atomic hydrogen is mainly generated by electron-SiH_4 collision and electron-hydrogen collision. When pressure was low (< 200mTor), microcrystalline film was growing while H_α may be slightly insufficient to achieve good crystallinity, due to less collisions therein smaller v_{th}. After increasing pressure (300-400mTorr), the adequate amount of atomic hydrogen contributed to crystal nucleation at the beginning of deposition, leading to improved crystalline percentage. When pressure kept increasing, atomic hydrogen more likely converted to precursors, which would promote the growth of porous, hydrogen rich amorphous phase, thus reducing conductivity. It's reported that higher H concentration has been measured in samples deposited at high pressure[63]. Moreover, the deposition rate at 400mTorr was lowest which agreed with highest crystallinity, and the quick increase with pressure fits well with amorphous phase growth assumption.
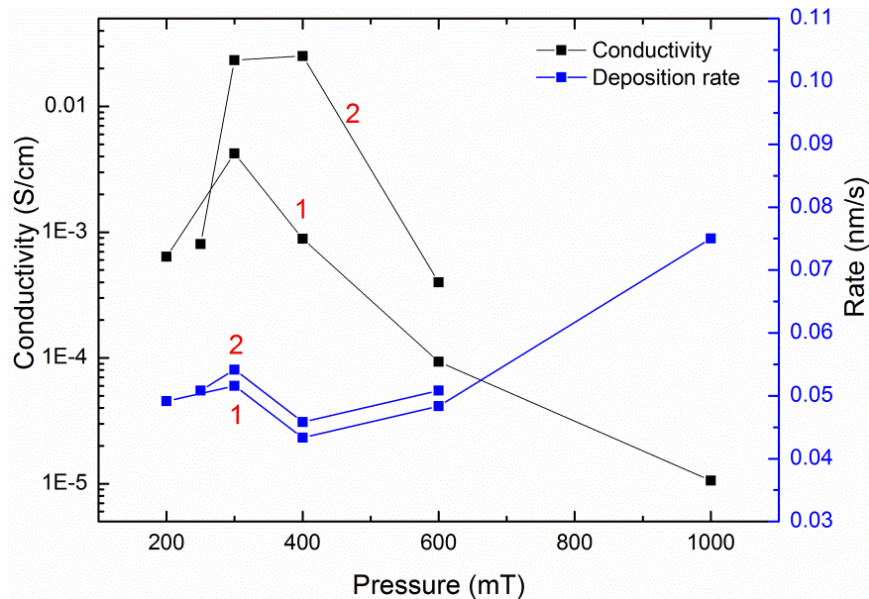
Figure 3-10 Effect of chamber conditions on the conductivity and deposition rate on p-type μc-Si:H film. Sample series 1 and 2 were deposited before and after chamber conditions stabilized.

Fig 3.11 depicts the effect of power on electrical properties and deposition rate. Sample sets a and b were deposited with different pressure 600mTorr and 300mTorr respectively, with other parameters the same (SiH_4 =2sccm, B_2H_6/ SiH_4=0.009, H_2 = 400sccm, temperature=180ºC), also, series a were deposited before chamber stabilized, whereas series b were after. Apparently, high power would give high radical densities thus high deposition rate, which was nearly linear dependence of power as shown in Fig 3.11. There existed a power zone (55-65W) for optimized film quality with good crystallinity and thus conductivity, since high power would cause loss of crystallinity and favor the growth of amorphous phase [62]. After optimization of deposition parameters, the highest conductivity for 300nm film was 7.1E-2S/cm with power 56W, pressure 300mTorr, B_2H_6/ SiH_4 0.021 and H_2 400sccm at 180°C.
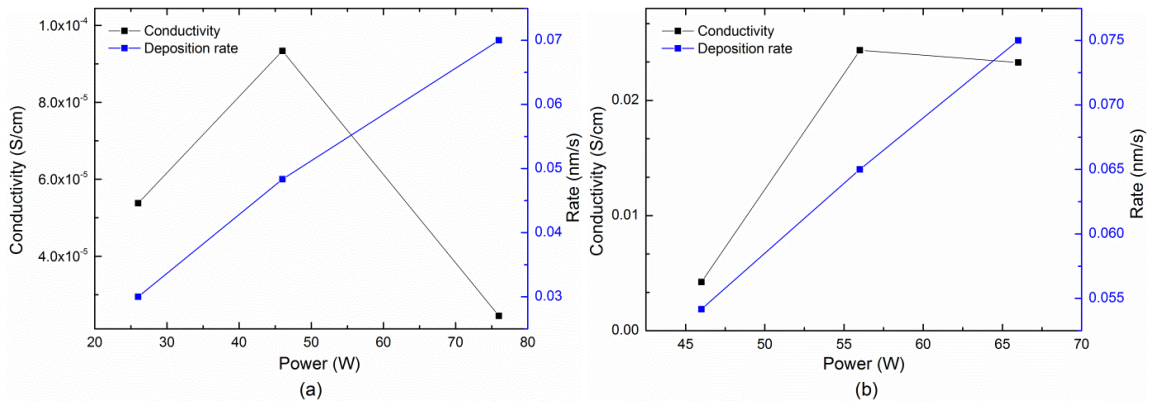
Figure 3-11 Effect of rf plasma power on the conductivity and deposition rate on p-type µc-Si:H film, (a) deposited at 600mTorr before chamber conditions stabilized, and (b) deposited at 300mTorr after chamber conditions well established.

Annealing effect has also been studied. The sample was deposited at 180 ºC for 20 minutes, and then annealed at 200ºC in N_2 atmosphere for one hour. The conductivity increased from 4.44E-2S/cm to 1.30S/cm, two magnitudes higher. One possible explanation originates from thermally activated annihilation and formation process of Si-H-B complex[59]. Boron dopants could easily react with silicon grain and achieve substitution doping. Hydrogen easily got involved in the unsaturated Si-B bonds and formed the neutral Si-H-B complex, which means boron was inactive in such a state. In this configuration, B-H bond was much weaker than Si-H bond, and would be easily broken, converting boron to active dopants, therefore, increasing conductivity. Y.Sobajima et al. [64] have compared the infrared-absorption spectra of B-doped µc-Si:H films as deposited and after annealing,

and found that the B-H-Si complex had disappeared after annealing in 200ºC in N_2 atmosphere, which confirmed the activation of boron by thermally annihilated Si-H-B complex.

Chapter 4

ICP deposition and characterization of μc-Si

4.1 Introduction

Thin film microcrystalline silicon (μc-Si) is widely used for the fabrication of high speed thin film transistors, and stable, high-efficiency solar cells. In these applications, the key issues are low deposition rate and high processing temperature. Normal plasma deposition employs high H_2 dilution (98%~99%) which greatly reduces deposition rate.

Hot wire (HW) CVD is alternatives to the conventional plasma deposition. High rate μc-Si films have been deposited by HW CVD deposition, while lack of low energy ion bombardment in this method is believed to result in relatively poor film quality. The detailed nucleation and growth process is still controversial. One possible model is suggested by Matsude et al.[65]. The growing surface is fully covered by bonded hydrogen due to high H_2 dilution reactant gases and the H-recombination would produce local heating, both of which will enhance diffusion of precursors and find a energetically stable site to grow.

Inductively coupled plasma (ICP)-CVD, as a "remote plasam" tool, has much less ion bombardment on the deposition surface compared to direct plasma rf PECVD, because the plasma generation region is separated from film deposition region, and reactant particles diffuse to deposition surface rather than accelerates in a electric field and hit on the surface which is the case in direct plasma chamber like conventional PECVD tools. Moreover, the ion density in ICP is generated by inductive coupling, much higher ($\sim 10^{12} cm^{-3}$) than that traditional capacitively coupling generated in PECVD. The high plasma density and low ion bombardment on the substrate facilitate the deposition of device-quality μc-Si films with rapid growth from low hydrogen diluted silane gas.

4.2 Experiment setup

In this chapter, a novel change of a novel ICP chamber modification is proposed for deposition of low-temperature μc-Si films at high growth rates using the pure silane gas precursor. As recently shown by B.Strahm et al.[66], the hydrogen-dominated plasma which is essential for deposition of microcrystalline films can alternatively be obtained by a strong plasma depletion of the pure silane gas. In this plasma condition, the released H_2 gas from the film surface has significantly higher partial pressures compared to the silane gas precursor. Here, the film surface area is considered the chamber

walls exposed to the SiHα radicals. As Fig 4.1 shows, in the modified system, a grounded plasma showerhead is placed between the high density plasma source and the bottom grounded electrode where the substrates are mounted. The grounded plasma showerhead plays three important roles: (i) increasing the H_2 partial pressure by increasing the plasma exposed surface, (ii) weakening the ion bombardment, and (iii) increasing the fractional ionization capacity.

In the proposed system, the plasma is excited by an inductively coupled coil connected to 13.56 MHz RF generator. The plasma showerhead pattern has been optimized to ensure the film uniformity and the easy flow of the precursors. Three adjustable stands completely separate the plasma source from the chamber deposition compartment. The films for structural, electrical and optical measurements were deposited onto 0.5mm thick Corning 1737 glass substrates. Raman spectroscopy was employed to estimate the crystalline fraction (XC). Raman spectra were measured in the backscattering geometry using a Renishaw micro-Raman spectrometer with a 488nm excitation laser line. Transmission and reflection spectra of μc-Si films were measured using a Perkin Elmer lambda 1050 UV–vis spectrophotometer and the film thicknesses extracted from these measurements following the procedure of Ref[45]. Samples for conductivity measurement were prepared by sputtering coplanar Al electrodes through a shadow mask and photoconductivity was measured under an illumination close to the air mass (AM) 1.5 spectral distribution and an intensity of $100mWcm^{-2}$. X-ray diffraction (XRD) was performed with a PANalytical X'Pert PRO X-ray diffractometer (Source: Cu Kα1; Tube voltage: 50kV; current: 40mA).

Gas input

ICP plasma

ICP coils

Shower head plate

Separator plate

Plasma diffused
through separator plate

wafer

Insulator

Bottom Electrode

stand off
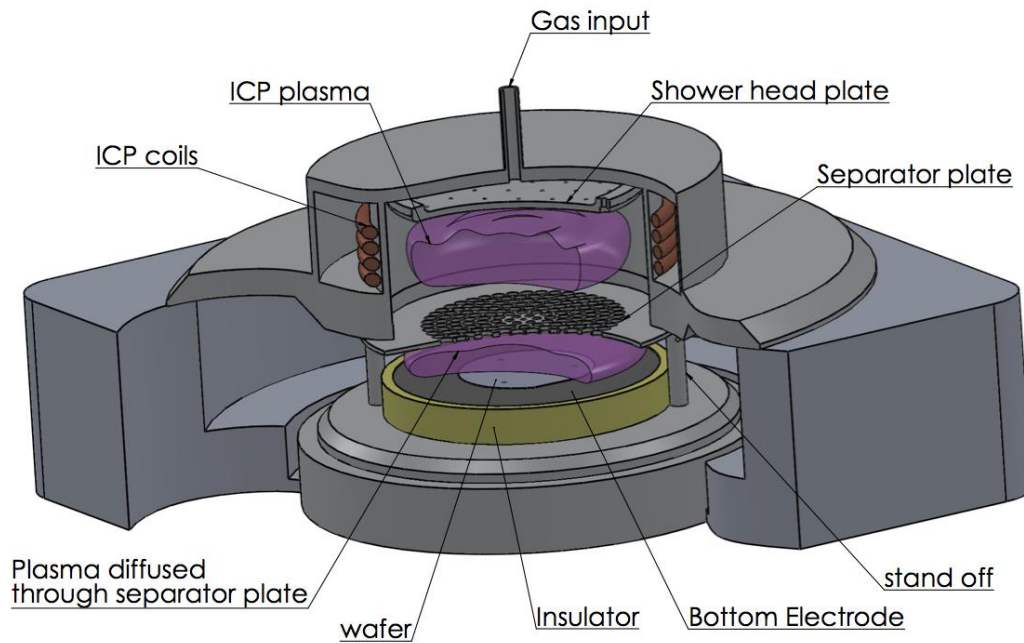
Figure 4-1 Modified ICP-CVD chamber with a showerhead between plasma generation region and
deposition region.

4.3 Results analysis

Fig 4.2 shows the Raman spectra of films deposited with and without plate in the chamber. The film
had a small crystalline peak and a wide amorphous shoulder when deposited without plate, however,
the crystalline peak became very sharp after placing the plate in chamber, which indicated the film
was crystallized. The effect of having plate may help to achieve high depletion of SiH_4, which favors
microcrystalline growth. Details of possible effect of plat in chamber have been explained in the
experiment part.
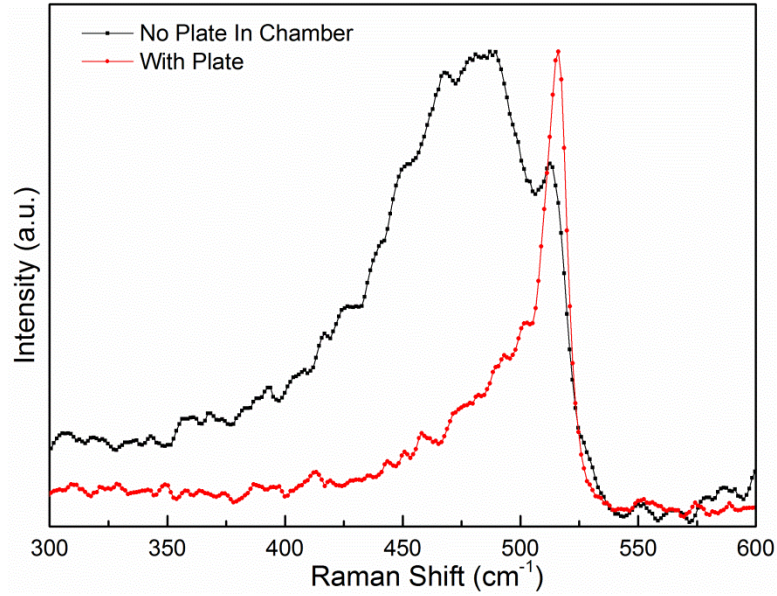
Figure 4-2 Raman spectra of films deposited with/without plate in the chamber.

Figure 4.3 shows the Raman spectra of μc-Si films deposited using silane gas flow rates of 20, 30, and 40 sccm at the substrate temperature of 180ºC. For all these depositions, pressure and power were kept at 5mTorr and 400W, respectively. The observed spectra were fitted with three Gaussians peaks centred at 480 cm^{-1}, 504-511 cm^{-1}, and 514-518.7 cm^{-1}, corresponding to the transverse optical (TO) phonon mode of the amorphous fraction and optical vibrational modes of Si nanocrystals, respectively. The crystalline volume fraction, Xc, was determined using relation

$$X_C = \frac{I_c}{(I_c + \eta I_a)} \tag{5}$$

where Ia and Ic are the integrated intensities of the amorphous (480 cm^{-1}) and crystalline (504-518.7 cm^{-1}) peaks, respectively. The ratio of the back-scattering cross section, η, is chosen to be 0.8. It was seen that silane flow rate of 20sccm result in a μc-Si film with crystalline fraction of 68% and deposition rate of 5.1 Å/s. In comparison with other μc-Si deposition techniques this growth rate is very competitive in terms of the gas usage which is an important factor in cost reduction of the deposition process. In conventional PECVD technique, the same growth rate can be achieved using relatively high hydrogen dilutions (>100sccm) and higher substrate temperatures (>250 ºC). To further increase the film growth rate, silane flow rate was increased to 30sccm. While the film growth rate increased to 6.2Å/s at this flow rate, the evaluated crystalline volume fraction decreases to 45% indicating suppression of crystalline growth. Additionally, the film becomes amorphous as the silane

39

flow rate increases to 40sccm (See Figure 4.3). It was observed that the deposition rate didn't increase by the same rate as the silane flow rate and so was not the H_2 gas density which was by-product of the deposited film. Here, the lower hydrogen dilution ratio was responsible for the suppressed crystalline fraction of the films with higher silane flow rate. Without the plasma showerhead, the deposited films with the same plasma conditions are all amorphous.
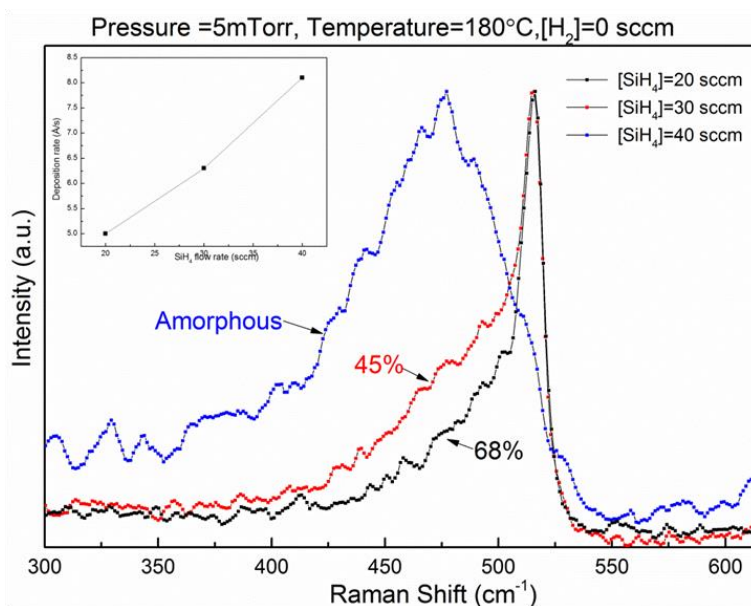
Figure 4-3 Raman with different SiH_4 flow rate.

Figure 4.4 shows the Raman spectra of the μc-Si films deposited at different substrate temperatures. Power, pressure, and silane flow rate are kept constant for all depositions. While the film deposited at 130ºC was amorphous, the crystalline peak at 520cm^{-1} started to appear for higher temperatures. It was seen that in the temperature range of 150-260ºC, X_c increased abruptly from 60% to 68% and then saturated at around 71%. This characteristic was fully compatible with previous observations and was explained by temperature dependence of H-elimination reactions on the growing surface. In order to study the temperature-dependent photosensitivity of the deposited films, photo- and dark-conductivity (σ_{ph}, σ_d) measurements were performed. As it is shown in Figure 4.5, with increasing the substrate temperature, both conductivities steeply increased at around 150ºC. Above this threshold value σ_{ph} and σ_d remained almost constant at 10^{-4} and 10^{-6} S/cm, respectively. This abrupt change in the conductivity values were attributed to the higher (and constant) crystalline fraction of the film deposited at the temperatures above 150 ºC.

40
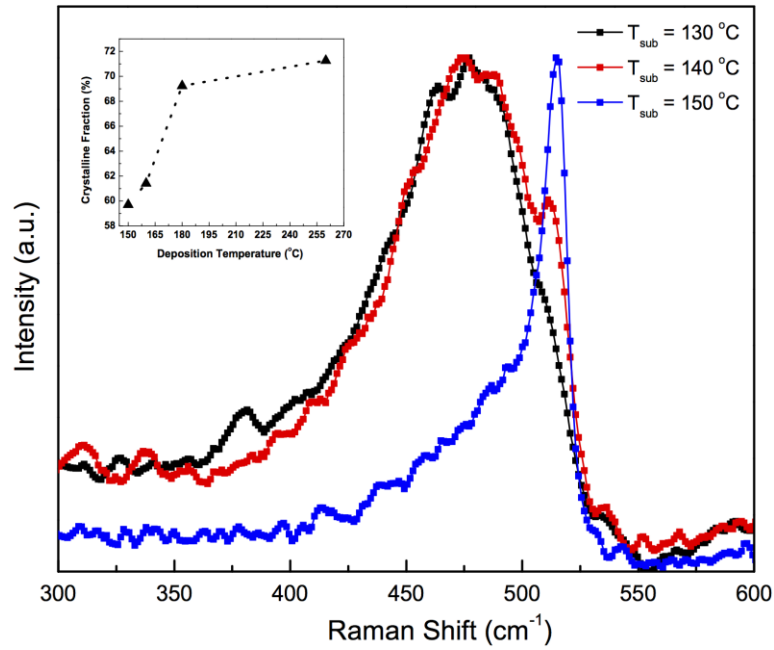
Figure 4-4 Raman and crystalline fraction of µc-Si:H as a function of temperature.
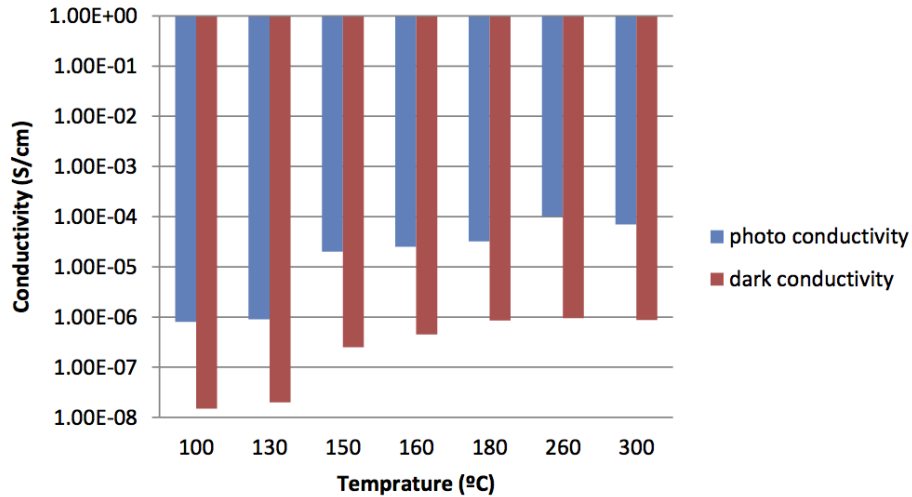
Figure 4-5 Photo and dark conductivity of µc-Si:H as a function of temperature.

To investigate the crystal structure, the XRD analysis of the film deposited at 180ºC was performed. Figure 4.6 shows the XRD spectrum of this film where three diffraction peaks corresponding to Si(111), Si(220), and Si(311) surfaces are distinguished from the broad background signal. The Al(111) peak is due to the Al electrodes deposited at the sample.
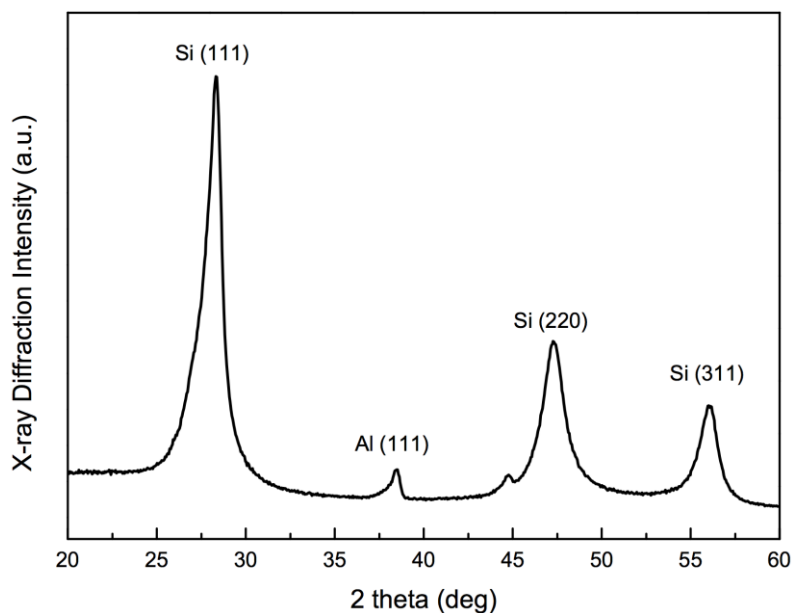
Figure 4-6 XRD results of μc-Si:H deposited at 180ºC.

In order to study the thickness-dependent structural and electrical properties of the μc-Si films, samples with different thicknesses (35-1051nm) were deposited at the substrate temperature of 180°C and silane flow rate of 20sccm. Figure 4.7 and 4.8 shows the variation of Raman, photo- , and dark-conductivity for this thickness series. As it is shown in Figure 4.6 the amorphous shoulder at 480 cm^{-1} was more prominent for the 35nm film compare to that of 1051nm film. The crystalline fraction of 44% for the 35nm film clearly showed the presence of a very thin incubation layer at the film/substrate interface. The calculated crystalline fraction showed saturation at the film thickness of 300nm which implies the formation of fully dense conical conglomerates[67]. Figure 4.8 shows the variation of photo- and dark-conductivity for the thickness series. Both photo- and dark conductivities showed small values for thicknesses <100nm and changed abruptly for thicker films. The observed abrupt change in conductivity was explained in terms of percolation theory by destruction of a percolation cluster composed of nanocrystallites as the layer thickness became comparable to the size of a crystallite. A maximum photoconductivity was observed for the film with thickness of 300nm. At this thickness, it is believed that the film structure composed of densed nanocrystallites passivated with amorphous tissue. As it is explained by[68], this structure shows the best photo properties.
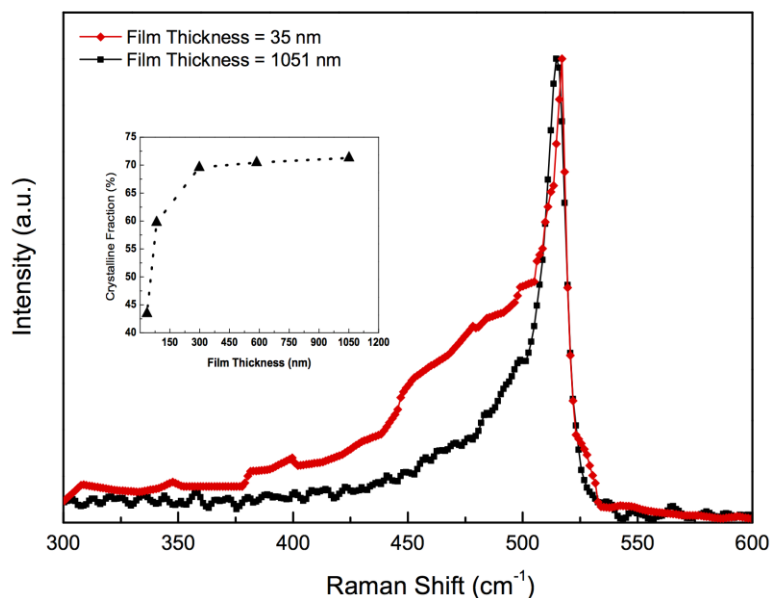
Figure 4-7 Raman and crystalline fraction of μc-Si:H as a function of film thickness.
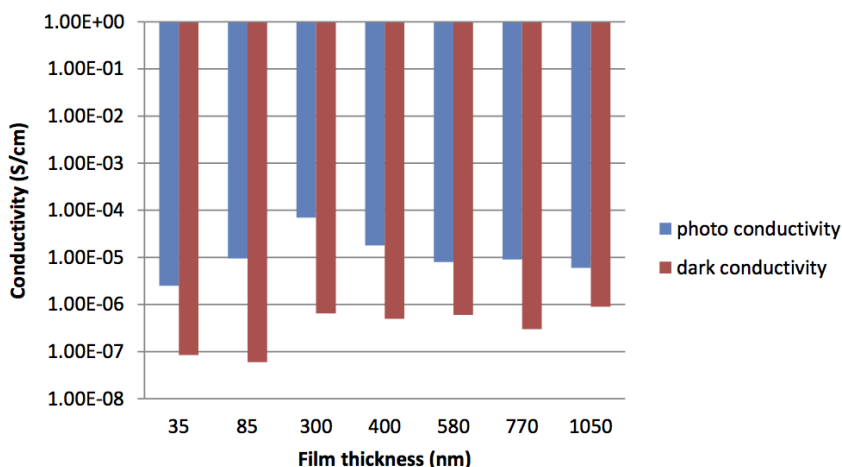
Figure 4-8 Photo and dark conductivity of μc-Si:H as a function of film thickness.

Additionally, it has been observed that the dominant ions in ICP at high power regime (>100W) are ionic species like SiH_X^+ and H_X^+[69], i.e. electron-induced SiH_4 dissociation/ionization. Due to the design of ICP chamber, the deposition region with a big area has lower pressure than the confined plasma generation region, which favors the diffusion of these species to film growing surface. When passing through showerhead, only one third goes through successfully and contributes to film growth which may possibly explain microcrystalline formation. Furth characterizations need to be studied in order to clear the formation mechanism of microcrystalline silicon in ICP.

43

Chapter 5

ICP deposition and characterization of a-SiGe:H

5.1 Introduction

Silicon has been the predominant semiconductor material and its alloys have also drawn considerable attention both in lab and in industry. Among alloys with other group IV (C, Ge, Sn) elements, Ge gives the lowest bond mismatch ($\Delta l \sim 4\%$), whereas ~34% for SiC, and ~17% for SiSn[70]. Moreover, the bandgap of SiGe alloys could be tuned from ~ 1.1eV (pure a-Ge:H films) to ~ 1.7eV (pure a-Si:H films), which makes it a great candidate for full-spectrum absorption in solar cells, e.g. tandem solar cells. Usually, intrinsic a-SiGe layer is used in the middle or bottom cells to enhance long wavelength light absorption. Furthermore, a-SiGe:H has similar absorption coefficient with a-Si, avoiding the requirement of thick film as in the case of μc-Si. Several methods have been employed to develop a-SiGe film, such as HWCVD, LPCVD, sputtering etc. The main issue originates from the fact that a-SiGe has high defect density ($>10^{17}$cm-3)[71], which leads to pronounced degradation after light exposure, same phenomena observed in a-Si. It also limits the deposition rate of a-SiGe, since film quality will be impaired as a result of increased defect density, currently the rate is around 0.8~1Å/s or lower. Recently, high deposition rate has been reported by Q.H.Fan et al. with 4Å/s by rf PECVD[72]. They adopted high pressure (2-4Torr), relatively high RF power density (116mW/cm^2), and high H_2 dilution ratio (H_2:Si_2H_6=100:1).

5.2 Experiment setup

In this chapter, trial deposition of a-SiGe:H has been done on Corning Eagle XG glass substrates by ICP with an initial deposition rate up to 4.7Å/s, with very low pressure (5mTorr), low H_2 dilution (< 63%), and moderate power density. SiH_4, GeH_4 and H_2 were used as reactant gases. Three sets of samples were deposited with different gas ratio and temperature. Raman spectroscopy measurement was done in the backscattering geometry using a Renishaw micro-Raman spectrometer with a 488 nm excitation laser line. Cross-section view of transmission electron microscopy (TEM), annular dark-field scanning transmission electron microscopy (ADF-STEM) STEM, and energy-dispersive x-ray spectroscopy (EDS) were conducted by JEOL 2010 field emission TEM/STEM.

5.3　Results analysis

The dissociation of silane and germane is mainly due to collision with electrons in the absence or low dilution of H_2, and the most possible radicals are SiH_3, SiH_2, GeH_3 and GeH_2[73]. Radicals along with a very small amount of atomic hydrogen would diffuse to the growing surface and form films. Fig 5.1 shows the original Raman spectra of a-SiGe:H films with different deposition temperature. A strong photoluminescence background was observed with film deposited at 150ºC, and decreased when temperature increased. The PL background was believed from radiative recombination of electron and hole pairs[74]. It's strongly influenced by H_2 content in the film and experiences exponentially increase once H2 content exceeds a threshold value[75]. Herein, it was predicted that less H was incorporated into a-SiGe:H films at elevated temperature which was in consistent with other works[76]. Additionally, the activation energy of Ge-H bond is 0.30eV, lower than 0.76eV of Si-H bond[77]. As a result, Ge-H bond was more easily broke than Si-H bond and hydrogen were selectively taken off from Ge sites. So hydrogen in a-SiGe:H film was more preferably attached to Si sites in the form of SiH_2 or SiH. And SiH_2 would desorb hydrogen rapidly with temperature. Consequently, the preferential H attachment to Si induced more Ge dangling bonds than Si, which increased with high Ge content. The pl background was subtracted to avoid any adverse effect on further analysis, shown in Fig 5.2. Also, due to the nonconstant total Raman signal, the scattering intensity was normalized.

Fig 5.3 presents the modified Raman spectra of a-SiGe films. The three broad peaks 280, 390 and 480 cm^{-1} correspond to Ge-Ge, Si-Ge, and Si-Si transverse optical (TO) vibrations, respectively[78]. It was obvious that the film was SiGe alloys instead of a mixture of pure Si and Ge particles. The film deposited at 150ºC was mainly composed of Ge-Ge bonds, with some Si-Ge bonds, no evidence of Si-Si formation, which could be explained by lower activation energies associated with germanium deposition compared to those associated with silicon. Moreover, Ge has higher sticking coefficient which gives more chance for Ge-Ge bonds growth[79]. When precursors reached and got absorbed in the growing surface, they diffused to reactive sites and formed chemical bonds, while those with low sticking coefficients were more easily to be desorbed from surface, leaving a Ge-rich film in this case. When temperature increased to 300ºC, Si-Si bonds appeared and the intensity of Si-Ge bonds increased at the expense of Ge-Ge bonds because the sticking coefficient of Si radicals has been proved to increase with high temperature[80], and SiH_2 radicals has higher sticking coefficient than SiH_3, so it's relatively easy for SiH_2 radicals to stick to the open dangling bond sites whereas SiH_3

would move randomly in the growth zone and tends to react with atomic hydrogen to form SiH_2 and hydrogen due to the high cross section of such reaction[81]. By further increasing temperature to 400℃, both Si-Ge and Ge-Ge peaks increased slightly and peaks got wider, showing that a-SiGe alloy formation was thermally favored. Quite similar trend has been found when the flow rate of GeH_4-to-SiH_4 flow is 2, and Ge-Ge is as expected more obvious than Si-related bonds.
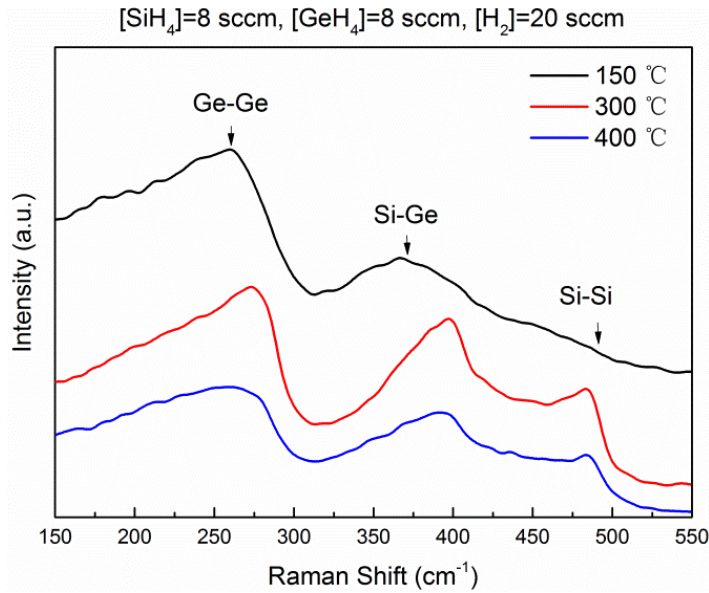
Figure 5-1 Raman spectra of a-SiGe:H samples with the flow rate of GeH_4-to-SiH_4=1.
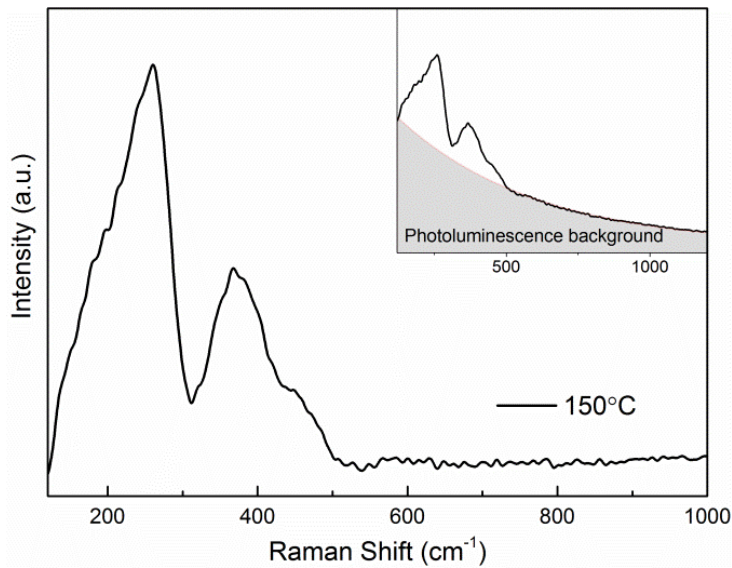
Figure 5-2 Raman spectra of a-SiGe:H sample at 150˚C after subtraction of PL background.

46
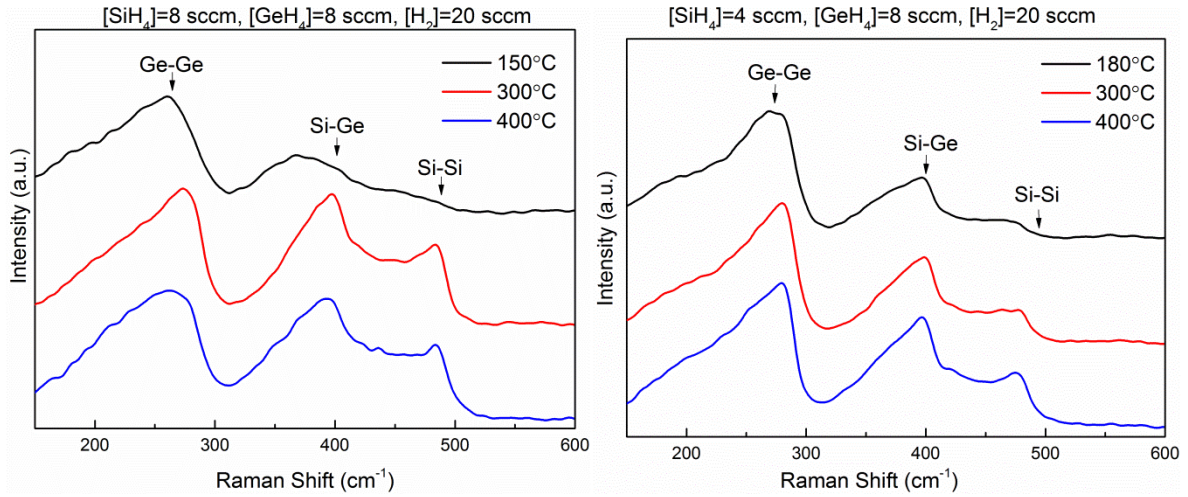
Figure 5-3 Raman spectra of a-SiGe with the flow rate of GeH_4-to-SiH_4=1(left) and GeH_4-to-SiH_4 =1/2 (right) after PL background subtraction and normalization

Although same amount of SiH_4 and GeH_4 gases have been introduced into ICP chamber in above set of samples, the film turned out to be slightly Ge-rich. Fig 5.4 shows the Raman spectra with half-reduced GeH_4 flow rate deposited at different temperatures. Ge-Ge and Si-Ge peaks were still obvious at low temperature although GeH_4-to-SiH_4 ratio was 2. Si-Si peak began to grow when temperature increased, indicating more Si was incorporated at high temperature. Moreover, the Si-Si peak was located around 500cm^{-1} which indicated possible crystallization in the film, and peaks exhibited red-shifting which confirmed increased Si content and could be used to calculate Ge percentage in the film by equation[82]:

$$y=520-70x \tag{6}$$

where y is the Si-Si peak position and x is the fraction of Ge in the bulk. The estimated Ge content is 36.2%, 33.5% and 32.2% respectively.

47
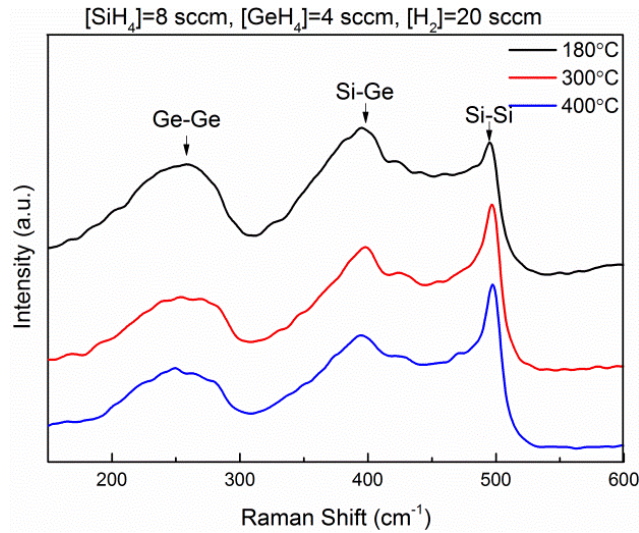
Figure 5-4 Raman of a-SiGe:H film with the flow rate of GeH$_4$-to-SiH$_4$=2 .

In order to obtain the distribution of Si and Ge along growth direction, cross-section STEM analysis was conducted on film deposited at 300ºC, and shown in Fig 5.5. The elemental line scanning profile provides a semi-quantitative estimate of composition (%wt). It was clear that the film was slightly dense close to substrate, and direct evidence of structural inhomogeneity was observed as dark region in TEM image (Fig 5.6). Fig 5.6 shows the EDS measurements on sp 2 and sp3 which were labelled in the cross-section TEM image. Main contributions are from silicon

[Si-K($E_{\alpha1}$=1740eV, $E_{\beta1}$=1832eV)], and germanium [Ge-L($E_{\alpha1}$=1186eV, $E_{\beta1}$=1216eV),

Ge-Kα($E_{\alpha1}$=9885eV) and Ge-Kβ($E_{\beta1}$=10,981eV)][83].

Fig 5.7 shows the microstructure has columnar shape. The bright columns were presumed low-density, void-rich, and mostly probably with high dihydride-to-monohydride ratio, both would lead to poor electronic properties[83]. The columnar-like microstructure was suggested caused by a reduced average surface mobility of the depositing radicals as a result of high fractions of germane in the plasma [84]. The dense island coalescence was hindered and self-shadowing induced column formation visually. It turned out the film was mostly amorphous with some nano-scale crystallites embedded by HRTEM (Fig 5.8). Most crystallites were distributed located close to interface which gradually disappeared and the film became more amorphous near surface. The dimension of crystallites varied from roughly 3nm to 10nm. The insets were live Fast Fourier transform (FFT) images.

48
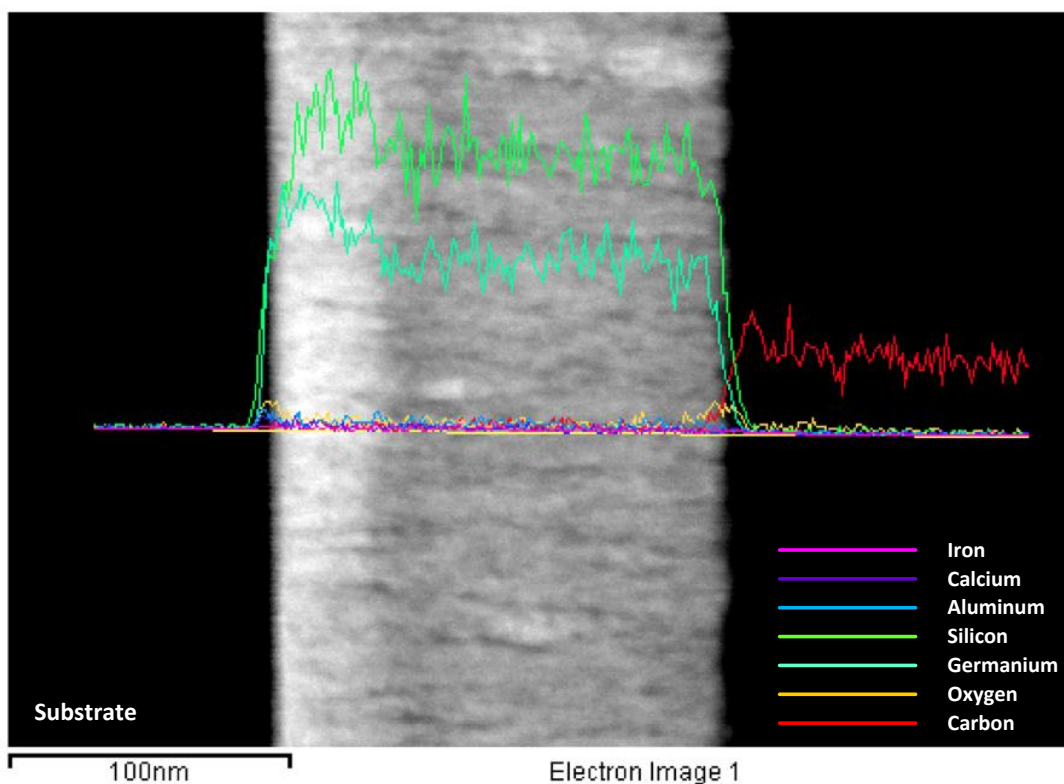
Figure 5-5 STEM micrograph of the a-SiGe:H film on glass substrate.
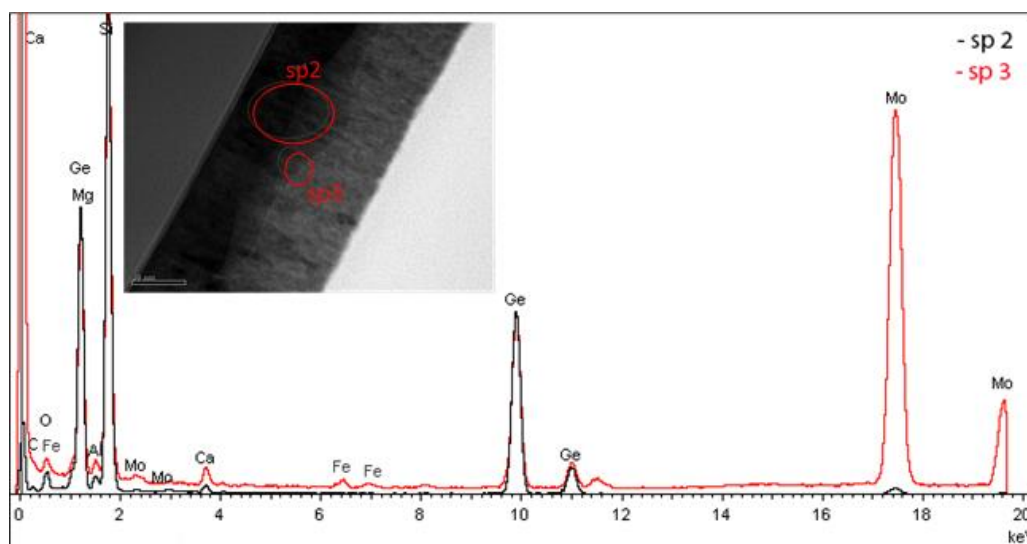
Figure 5-6 EDS spectra for a-SiGe:H sample with the flow rate of GeH_4-to-SiH_4=1/2 at 300°C
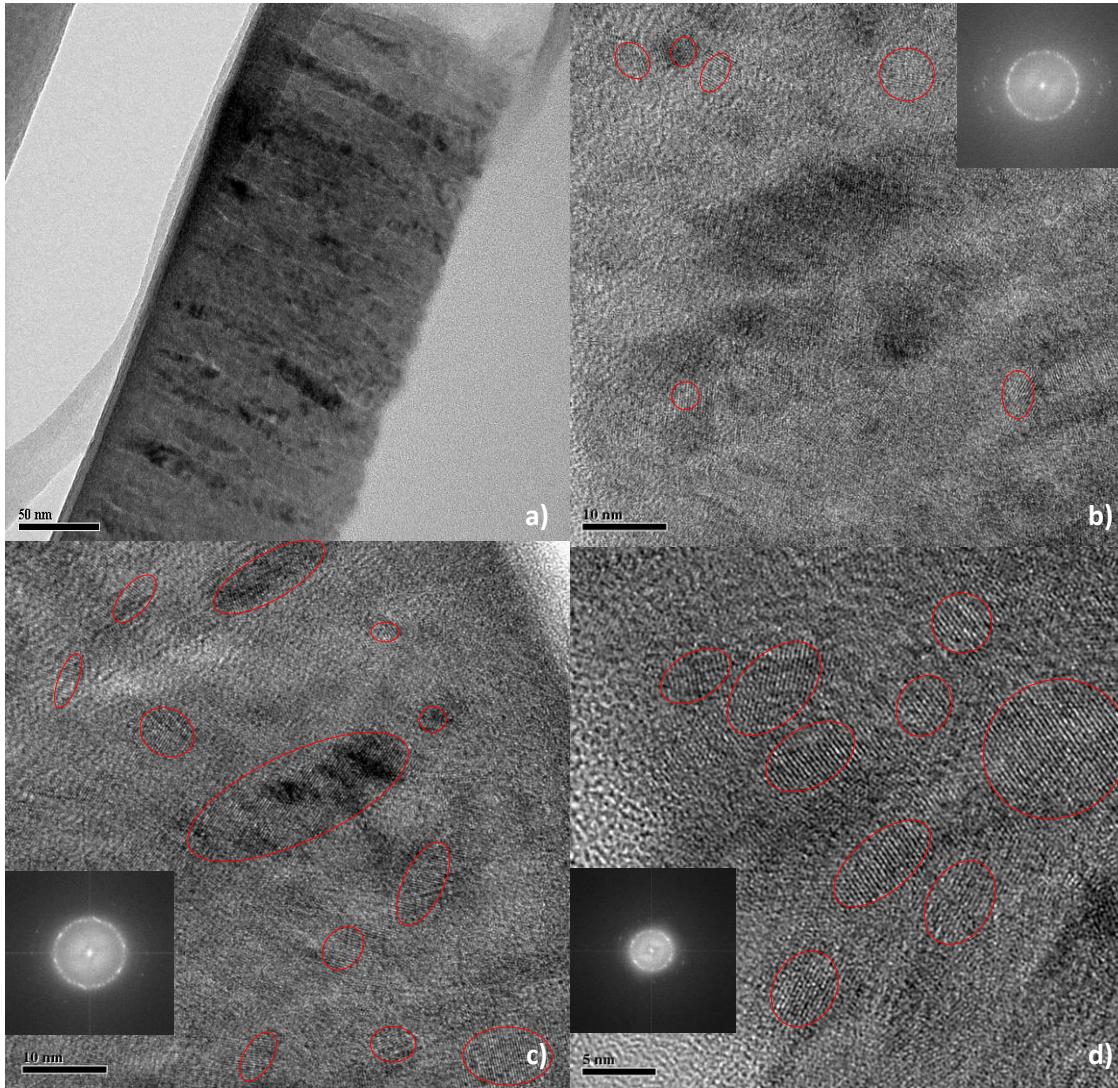
Figure 5-7 (a). Cross-section TEM micrograph of a-SiGe:H sample with SiH_4=8sccm, GeH_4=4sccm, H_2=20sccm at 300˚C, (b) & (c) HRTEM of region b and c, d) HRTEM near substrate.

The energy bandgap Eg can be determined by Tauc plot, which was a very effective method to analyze amorphous thin film materials. Fig 5.8 presents Tauc plot for one group of a-SiGe samples, where the intercept with x axis gives Eg values. The three regions give some information about band structure[85]. In the first extended-to-extended state transition region, the absorption coefficient is above 2×10^4 cm^{-1}, and can be described by equation:

$$(\alpha h\nu)^{1/2} = B(h\nu - E_g) \qquad (7)$$

where α is the absorption coefficient (cm^{-1}), $h\nu$ is the photon energy (eV), B constant, Eg the bandgap. The 2nd band-tail states transition range is also known as Urbach edge which spans a few tenths of an eV both above and below the optical bandgap Eg. The transition mainly occurs between valence tail states and extended conduction states. The characteristic Urbach energy can be calculated by the slope of absorption coefficient vs photon energy plot. The 3rd is the defect-to-extended state transition range where the integral of absorption coefficient is related with density of states associated with dangling bonds or similar defects. The transitions are most probably between defects and extended states of conduction bands. It can be seen that the optical bandgap decreases monotonously from 1.63eV to 1.42eV when temperature increases, which also agrees with other reports[86]. Fig 5.9 summarizes bandgap for all three groups of samples. Clearly, with increased temperature, bandgap decreased gradually. And it increased by increasing SiH$_4$-to-GeH$_4$ ratio.
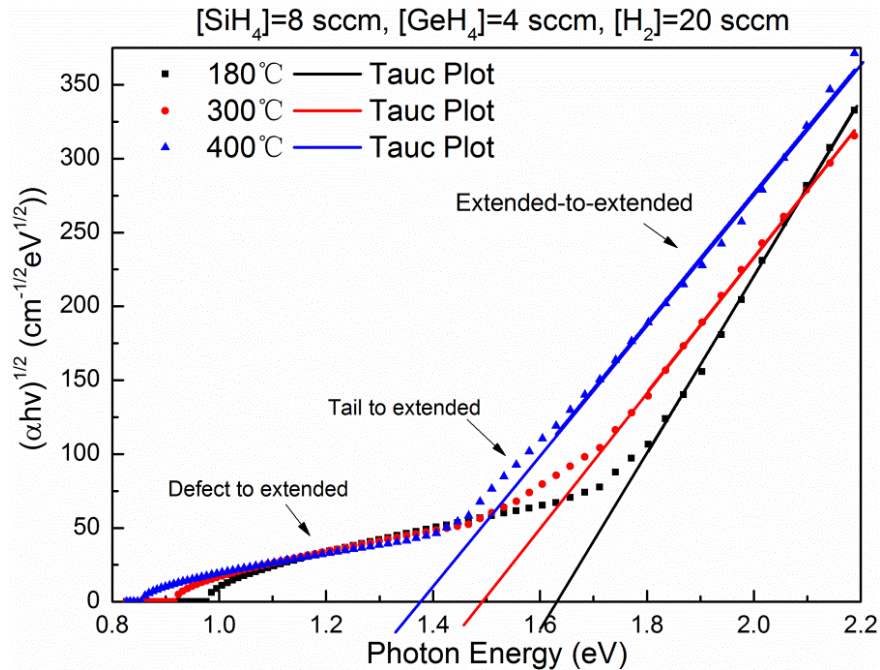
Figure 5-8 Tauc plot of a-SiGe:H with band states labeled.

51
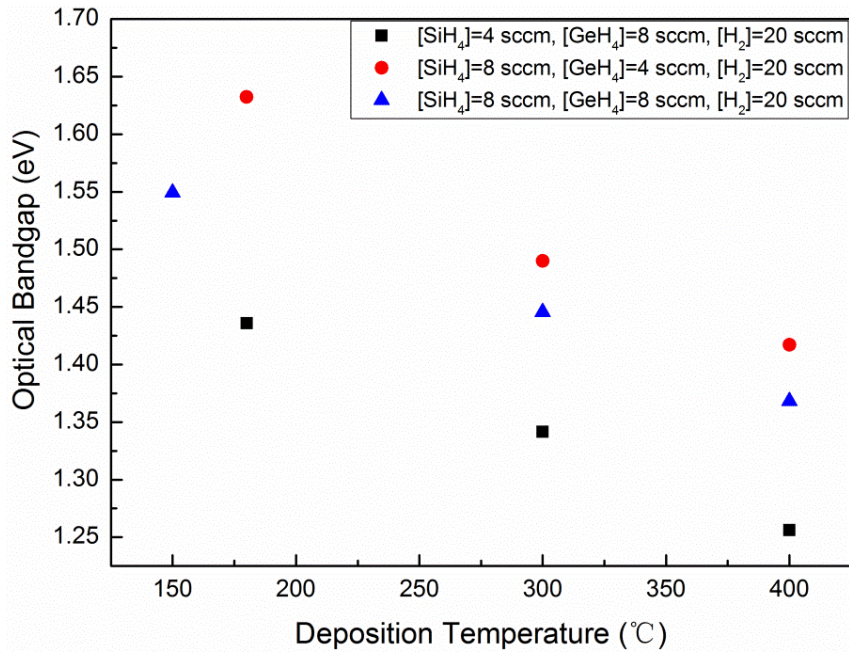
Figure 5-9 Optical bandgap of a-SiGe:H with different SiH_4 –to-GeH_4 flow rate and temperature.

Chapter 6

Fabrication and characterization of proto-type thin film solar cells

6.1   Introduction

In this chapter, several heterojunction solar cells on silicon substrates will be introduced. Compared to conventional c-Si solar cells in industry, heterojunction cells require shorter thermal treatment time and lower temperature, thus greatly reducing thermal budget (Fig 6.1), also, bowing of thin wafers is avoided which makes it possible to use very thin wafers. Moreover, the lifetime degradation of minority carriers is inhibited and therefore low quality c-Si wafers could be employed [71].
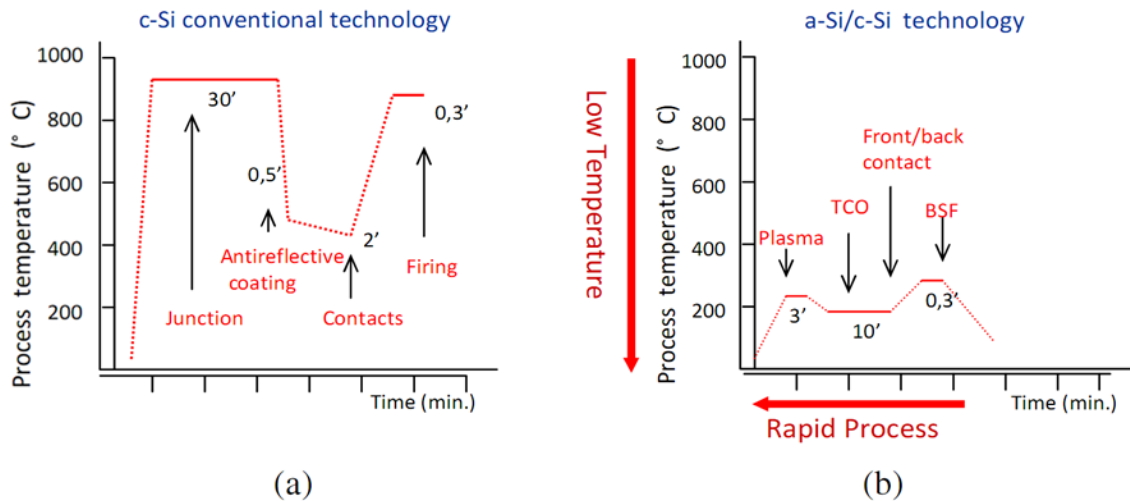
Figure 6-1 Comparison of thermal process in c-Si and a-Si solar cells[71].

Up to now, the record efficiency of HJ solar cells is 23.0% by Sanyo on CZ n-type c-Si substrate, with production efficiency around 20%[87]. The CZ n type c-Si substrate is costly, and the low doping efficiency of p type a-Si:H makes it challenging to form p^+ a-Si:H/TCO tunnel junction with n-type TCO at the emitter. Meanwhile, the development of HJ on p type c-Si substrate has drawn much attention. The p-type c-Si is widely available including solar-grade mono-crystalline and multi-crystalline Si wafers. And highly conductive n-type a-Si is more achievable than p^+ a-Si:H. The highest reported efficiency on p-type Si was 17.4% by PECVD[88], and 19.3% by hot-wire CVD[89]. In this report, HJ cell on p-type substrate was analyzed first followed by some trials on n-type Si introduced briefly.

6.2 Experiment setup

Fig 6.2 shows the schematic structures of heterojunction (HJ) solar cells in this work. No anti-reflection coating or back reflection or other light trapping schemes was used. The p type c-Si wafer was CZ wafer, with resistivity1-2Ωcm and thickness around 300μm. The wafer was RCA1 and RCA2 cleaned, HF passivated right before going into chamber. A very thin intrinsic a-Si layer was deposited first which would reduce wafer surface defect density by hydrogenation, successively the n-type a-Si emitter was deposited to set up electric field. On top of a-Si layers, Al doped Zinc Oxide (ZnO:Al) was sputtered which acted a transparent conductive layer, there was no other metallic contact to collect charge carriers which would be further discussed later. On the back side, aluminium was used as back contact.

200nm	AZO
20nm	n+ a-Si:H
15nm	i a-Si:H
300μm	c-Si wafer p type, CZ, <100>
300nm	Al
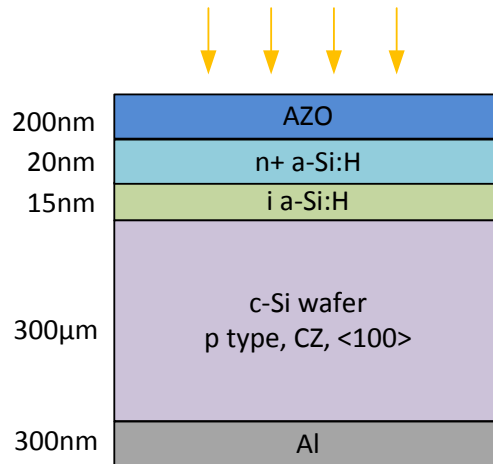
Figure 6-2 Schematic structure of heterojunction cell on p-type c-Si wafer.

6.3 Results analysis

A comparison of external quantum efficiency (EQE) of HTJ cells with and without textured substrate was given in Fig 6.3. For non-textured HJ cell, the interference fringes with deep valleys and tall crests were observed due to smooth interface between layers. The maximum EQE was 86.7% achieved at 570nm which was very good considering not any light trapping schemes were employed. When HJ had a textured substrate, those interference fringes disappeared as expected. The EQE became a smooth curve with maximum value 77.3% near 650nm. The current density of both cells is very similar, $26.23mA/cm^2$ and $26.73mA/cm^2$ for non-textured and textured cells respectively. Fig 6.4 presents the SEM image of textured wafer surface. The surface coverage of pyramid was close to

100%, and size of pyramids was around 1 to 10μm. The present of pyramids would greatly reduce surface reflection, from 30% to around 10% at long wavelength region and from 60% to 30% at short wavelength region. The reflected light has more chance to bounce back onto the surface for absorption. It's reasonable that textured cell has better short wavelength EQE due to the reduced refection, while not much improvement in the whole range. EQE data has proved that the good p-n junction has formed between n-type a-Si and p-type substrate.
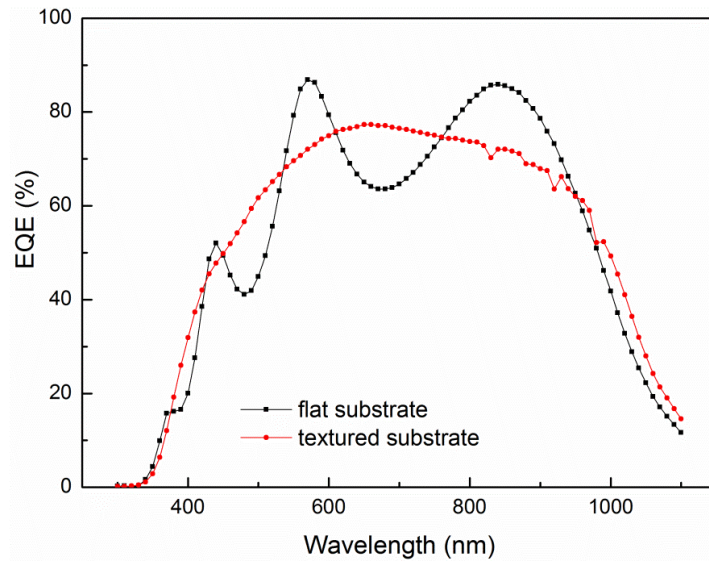
Figure 6-3 External quantum efficiency of textured and non-textured heterojunction cells.
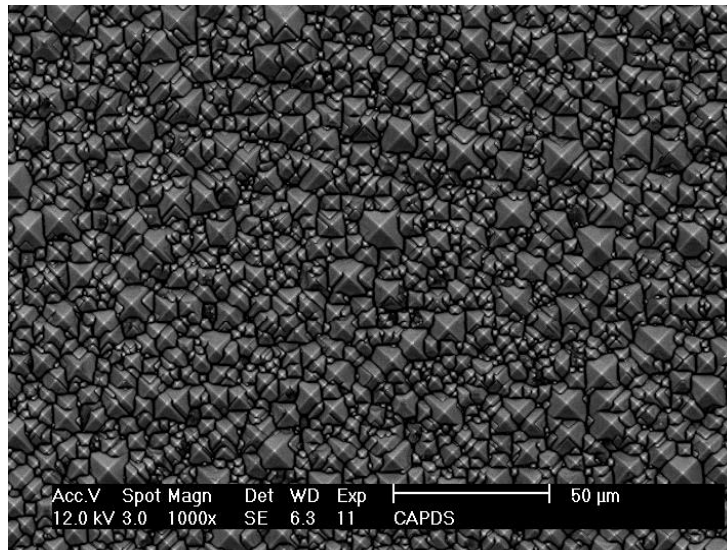
Figure 6-4 SEM image of textured c-Si surface

55

Lift-off process was employed to add aluminium fingers and busbars on top of ZnO:Al layer in order to reduce series resistance. The schematic structure was shown in Fig 6.5. However, the addition has deteriorated the EQE at short wavelength range, shown as red curve in Fig 6.6. It could be explained by degraded ZnO:Al layer after lift-off process.
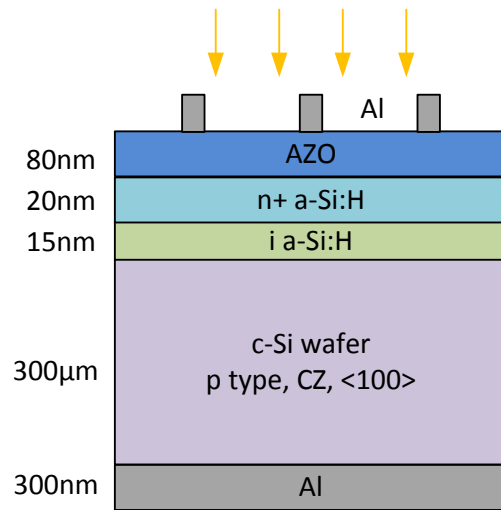
Figure 6-5 Schematic structure of heterojunction cells with Al fingers.
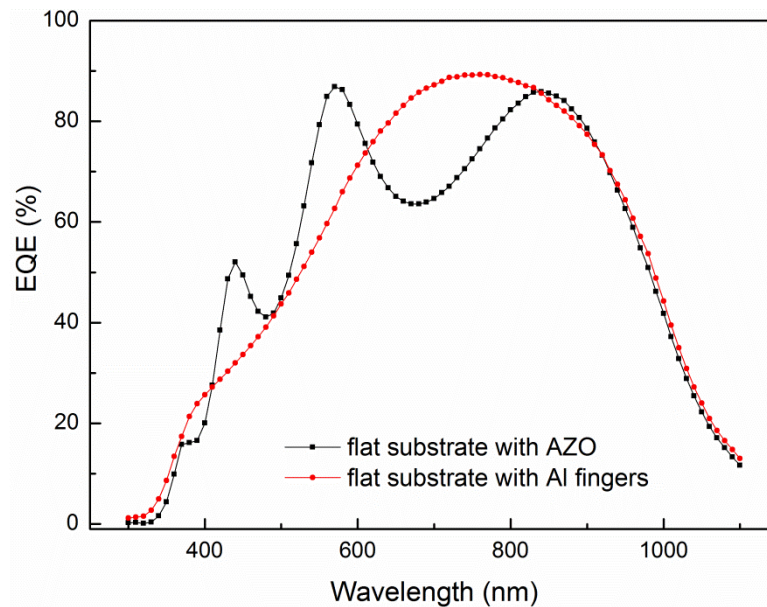
Figure 6-6 EQE of heterojunction solar cells with one 200nm layer of ZnO:Al layer (black curve) and Al fingers with 80nm ZnO:Al (red curve) as front contact.

It's reported that photoreisit developer and removal will attack ZnO:Al layer, reduce its transparency and increase resistivity[90]. Negative AZ nlof photoresist and AZ developer were used to form pattern, and aceton acted as "stripper" to remove photoresist and undesired parts. Fig 6.7 shows microscopy images of two sets of developed pattern with different developing and stripping time. The first sample was developed for 1 minute (Fig 6.7a) and had nearly vertical side walls. Consequently, metal was deposited on side walls as well when depositing contacts, and when it came to removal, the all-connected metal made it really hard and took very long time. Shown in Fig 6.7b the sample has been in aceton for half an hour and none of single cells was successful. The edge got peeled off due to large contact area with aceton, some fingers pumped up whereas the rest were still adhered, leaving no hope for successful lift-off contacts. In comparison, the other sample was developed for 2 minutes, and showed double-line clearly on the edge as an indication of steeply developed sidewalls (Fig 6.7c). And all fingers got off less than 1 minute when immersed in aceton (Fig 6.7d). The ZnO:Al surface got less compact and had more pore present after lift-off process, which may act as recombination center and trap carriers. It in turn could explain the reduced short wavelength EQE since short wavelength light has low absorption depth and is absorbed near the surface. The roughed surface may also be the reason for smooth EQE curve.
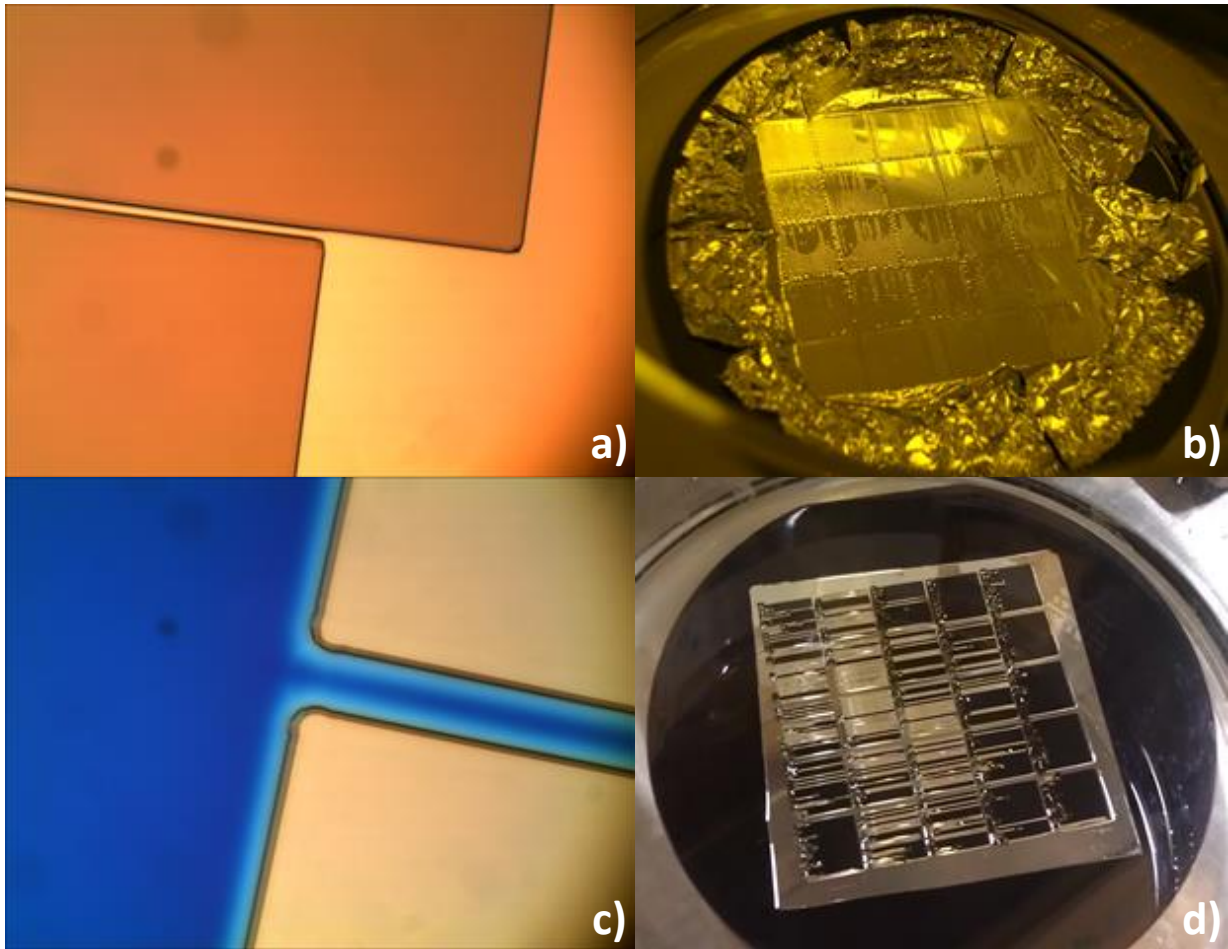
Figure 6-7 Lift-off samples a) developed one minute, b) after 30 minutes in aceton stripping, c) developed two minutes, d) after 1 minute in aceton stripping

Fig 6.8 depicts the effect of intrinsic a-Si layer thickness on EQE. One set of samples ZnO:Al as front contact, the other set has fingers and busbars either made of aluminium or silver. Both have observed EQE drop especially around 800nm. It's reasonable because more light-generated e-h pairs got recombined due to less-effectively passivated interface between intrinsic a-Si:H layer and substrate as a result of reduced i-layer thickness. The collected e-h pairs were decreased so as EQE which is defined as collected current over incident light energy.
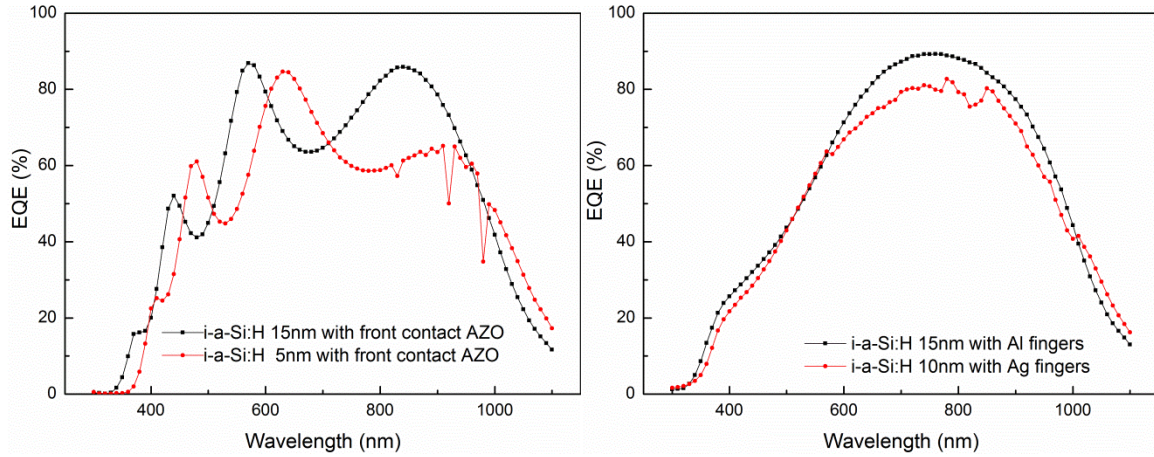
Figure 6-8 External quantum efficiency of heterojunction cells with different intrinsic a-Si:H layer thickness and different contacts. [91]

Moreover, dark IV measurement was conducted to further investigate the junction properties by Agilent combined with a dark box. The current-voltage relationship in a Si solar cell can be expressed as[92]:

$$I(V) = I_{0R} \left[exp \frac{q(V - IR_S)}{n_1 kT} - 1 \right] + I_{0D} \left[exp \frac{q(V - IR_S)}{n_2 kT} - 1 \right] + \frac{V - IR_S}{R_{sh}} + I_L \tag{7}$$

where I_{0R} and I_{0D} stand for recombination and diffusion saturation currents, n_1 and n_2 the ideality factors, k Boltzmann constant, T the temperature, q the electron charge, R_S the series resistance and R_{sh} the shunt resistance. Theoretically n_1 which defines the diffusion process within solar cells equals one, and n_2 is around 2 which reflects recombination in the depletion region. Fig 6.9 presents the semi-logarithmic I-V plot for 1cm^2 solar cell at room temperature. At low voltage range (0.05V to 0.2V), the current is primarily determined by shunt resistance. From 0.2V to 0.4V, the effect of electric field and depletion in the intrinsic layer becomes dominant. Then the current injection by diffusion appears importance from 0.4V-0.6V. The effect of series resistance turns more obvious from 0.6V upwards. The ideality factors were determined by doing linear fit at certain voltage range. The n_1 and n_2 turned out to be 2.3 and 3.3 respectively which indicated loss of photocarriers by recombination at the junction. In addition, the derivation of n_2 didn't count in interface and surface recombination for simplification which are critical for heterojunction cells.
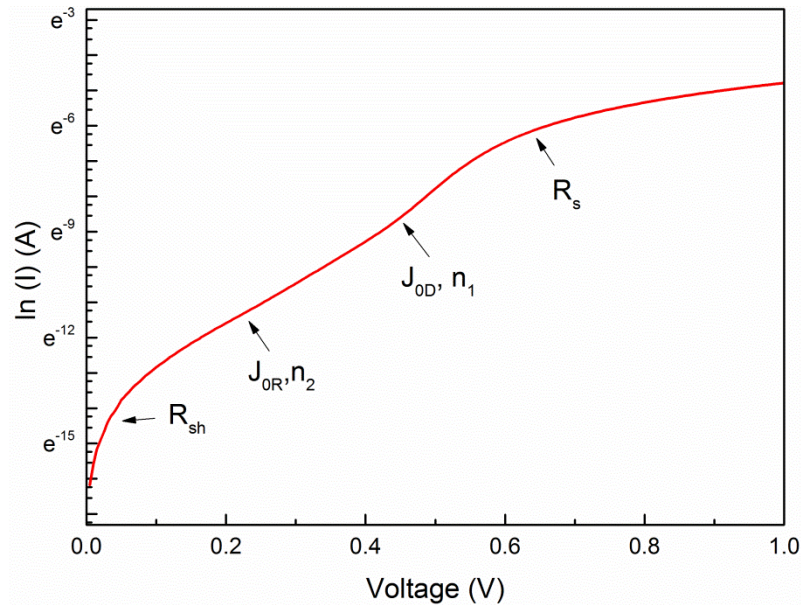
Figure 6-9 Dark IV of a heterojunction cell with area of 1cm^2, which has 15 nm intrinsic a-Si:H layer and aluminium fingers on the front surface.

When incident light was applied on the same cell, there was a deflection point in the fourth quadrant which severely reduced solar cell's fill factor thus performance, and it got worse with stronger light intensity (Fig 6.10). When at low reverse bias, the reverse current was limited by reverse bias voltage, and after reverse voltage has exceeded a threshold value, it became proportional to light intensity. Same phenomenon has been shown by M.Glatthaar et al.[93] which was believed caused by a slow charge transfer at one electrical contacts of the absorber layer. It's plausible at first thought considering the corroded ZnO:Al layer after lift-off process where additional charges injected from the good contacts were accumulated and transferred slowly. They also modeled same kink by reducing the extraction velocities for the charge transfer at one interface from 1000cm/s to 10^{-4}cm/s.
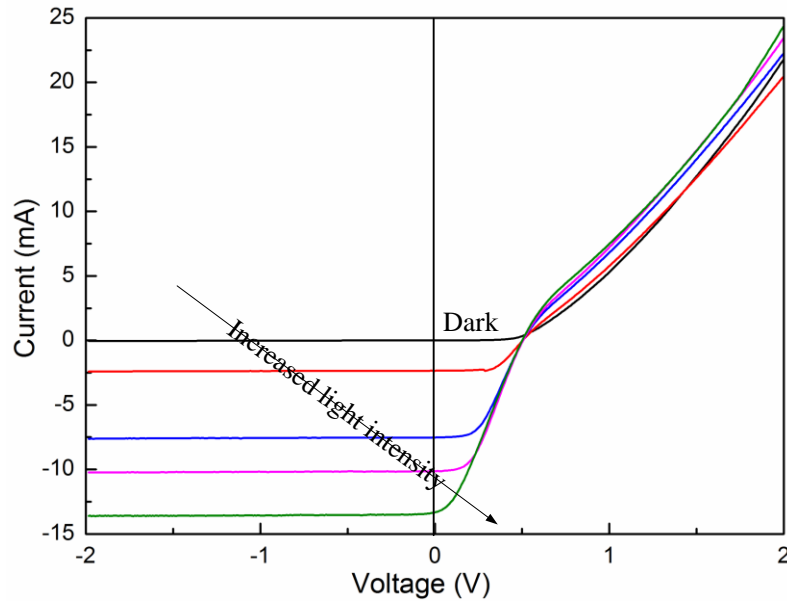
Figure 6-10 I-V curves of a heterojunction cell with area of 1 cm^2 at different light intensity.

However, same bump occurred in cells with titanium (Ti, 30nm) and silver (Ag, 800nm) as front contacts and silicon nitride (SiNx) as anti-reflection coating. At low reverse bias, carrier transfer was insufficient and limited by reverse bias, probably due to the present of an energy barrier between n$^+$ a-Si:H layer and front contact, which would be reduced by increasing reverse bias, so the current became limited by light. It's suspected that one energy barrier has formed between n$^+$ a-Si:H layer and contact. J.Loffler et al.[94] has observed same phenomenon in their tandem solar cells and mentioned it was caused by a counter diode formed between absorber layers. In order to analyze, the schematic band diagram of the front contact barrier height of HTJ (Ag/Ti/a-Si:H(n$^+$)/a-Si:H(i)/c-Si(p)) was shown in Fig 6.11. The intrinsic c-Si has electron affinity 4.05eV[92] with bandgap 1.12eV, and Fermi level was shifted up 0.53eV after doping by calculation[95], so the work function of p-type c-Si was 4.48eV (4.08eV=4.05eV+1.12eV/2 -0.53eV). And the work function of a-Si:H is 4.3eV fresh and 4.6eV with surface oxidation[96], and Fermi level never approaches closer than 0.2-0.3eV to the mobility edge [97] with a bandgap 1.7eV, so the work function of n-type a-Si:H would be around 3.65eV~3.75eV (3.75eV=4.3eV-1.7eV/2+0.3eV). And the work function of titanium is 4.33eV[98] , and silver is 4.35eV[99]. At equilibrium (Fig 6.11), a Schottky diode was formed between Ag and n$^+$ a-Si:H, with an inversion region due to higher work function of Ag (Schottky barrier). The Fermi level at n$^+$ a-Si:H was pinned at one energy rather than bended due to large numbers of surface states [100]. When forward bias was applied, on the one side, the built-in electric field was reduced and

minority carriers were swept across junction and became majority carriers to contribute to currents, while current collection at low bias was not effective due to the high Schottky barrier, and by increasing forward bias the reversion region decreased gradually, resulting exponentially increased forward current. When reserves bias was applied, electric filed in the junction was extended and enhanced, so drift current was reduced (less electron from p region to n region, and less hole from n region to p region), the tunnel junction between n^+ a-Si:H and contact became thinner and more states available in the Schottky barrier. So electrons would occupy low energy states first when illuminated, and would occupy high energy states by increasing light intensity. All would be transferred to metal contact if enough available states have been provided which would increase by increasing reverse bias. As a result, reverse current under high light intensity got saturated at an increased reverse bias voltage. The leakage current was mainly limited by tunnel junction between n+ a-Si:H and contact at low reverse bias, and become saturated proportional to light intensity when reverse bias exceeded one threshold value. So it's possible to explain the bump in IV curve by introducing a reverse diode caused by work function difference and it still works when it comes to cells with ZnO:Al contacts. The working function of ZnO:Al varies from 3.3eV to 4.7eV[101], depending on deposition process and composition. No relevant characterization has been done to get the work function. Fig 6.12 shows the band diagram assuming ZnO:Al with a lower working function than that of a-Si:H(n)was used. Ohmic contact was formed and the built-in potential in contacts has the same direction to that in a-Si:H(n) and c-Si(p). So the ZnO:Al in our case is suspected to high work function. In conclusion, the kink in IV curve could be explained by Schottky diode caused by working function difference. The open circuit voltage was 567mV in this case determined by solar simulator under AM 1.5 spectrum.
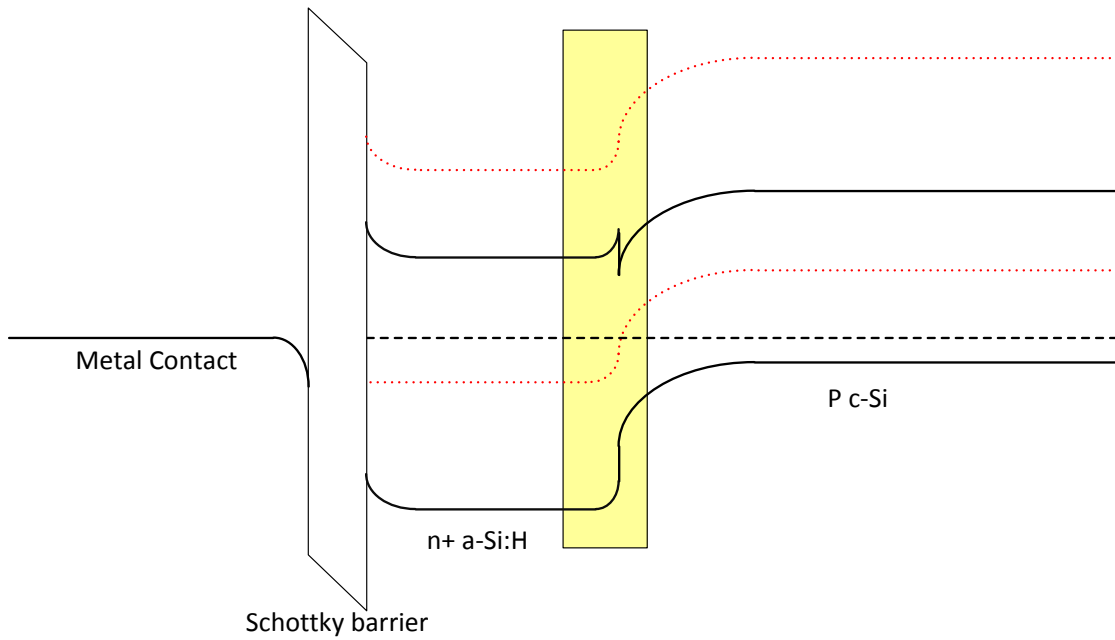
Figure 6-11 Energy band diagram when Schottky barrier is formed between emitter and metal.
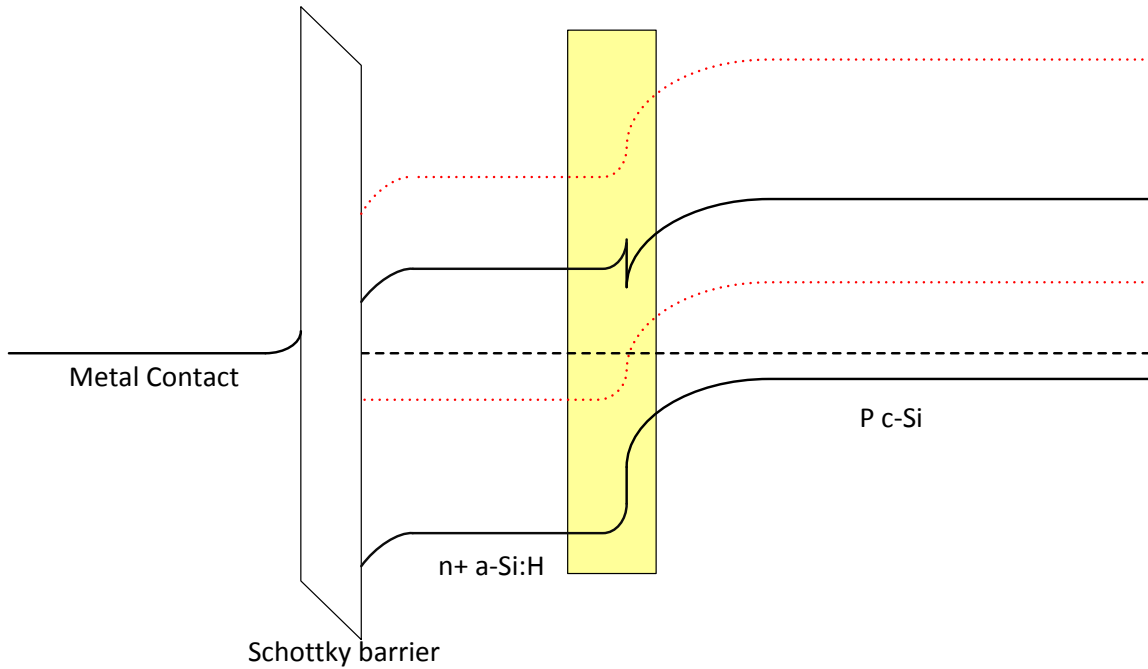
Figure 6-12 Energy band diagram when emitter and metal form ohmic contact.

Additionally, heterojunction solar cells have been tried on n-type c-Si substrate. Fig 6.13 presents the structure and EQE results. Although back surface field was applied, EQE was much lower than that

on p type Si substrate, most probably it was caused by the ineffective doping of p-type a-Si which greatly impaired junction properties. Due to the lack of finger and busbars, IV characterization wasn't conducted.

80nm	AZO
20nm	p+ a-Si:H
15nm	i a-Si:H
300μm	c-Si wafer n type, CZ, <100>
15nm	i a-Si:H
20nm	n+ a-Si:H
300nm	Al
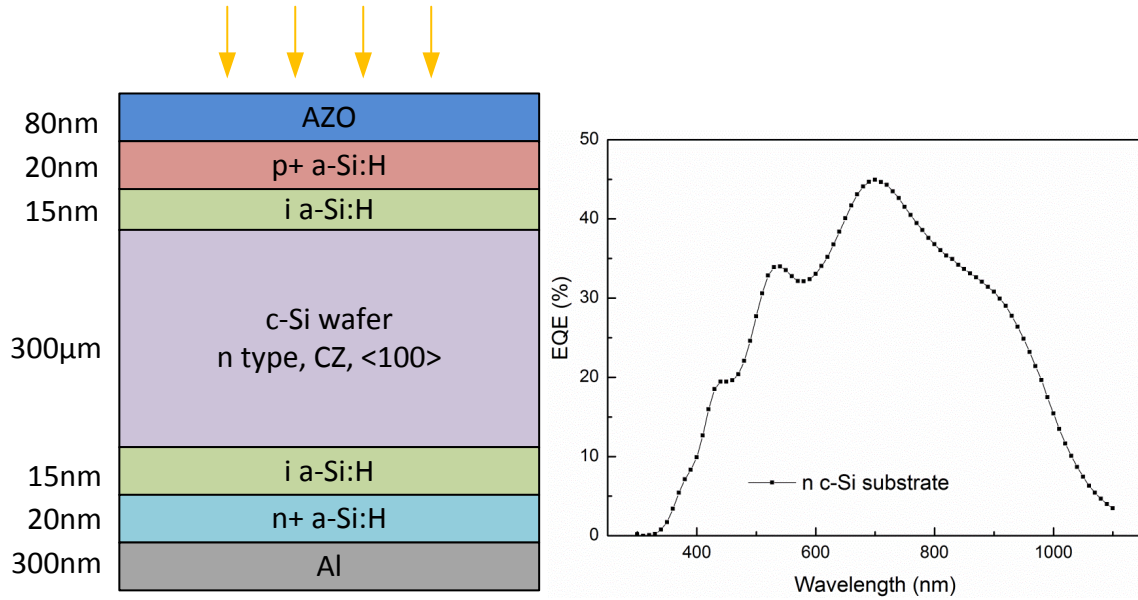
Figure 6-13 Structure of HIT cell on n type c-Si substrate and its EQE

Chapter 7
Summary

Comparing to conventional c-Si solar cells, thin film solar cells require less raw material, and can be deposited on cheap, flexible substrate, enabling building-intergrated applications. Also, monolithically manufacturing allows large area fabrication and continuous processing, which greatly reduces manufacture time, especially for CdTe solar cells which takes less than 2.5 hours from a bare substrate to capsulated module. It's also worth mentioning that thin film solar cells have better performance under harsh environment conditions such as high temperature, low light radiation.

Common tools for thin film deposition include PECVD, VHF-CVD, and HWCVD etc. Rf-PECVD is employed for a-Si:H and μc-Si:H deposition, both intrinsic and doped on 4 inch Corning glass wafers. High conductive n type a-Si:H has been developed at low temperature by pure SiH_4 and H_2-diluted PH_3. And n type μc-Si:H has achieved 17S/cm conductivity with 98% H_2 dilution at 180ºC. Correspondingly, p type μc-Si:H has been deposited by SiH_4, B_2H_6 with 99% H_2 dilution. The effect of B_2H6-to-SiH_4 ratio on conductivity and deposition rate has been investigated with highest conductivity obtained at B2H6-to-SiH4 from the range 0.010 to 0.025. Also, it's found that high power is required to activate boron dopants, a narrow power zone around 180mW/cm^2 has been used to get high conductivity, whereas 17mW/cm^2 for n type μc-Si:H.

ICP-CVD has been modified to achieve high deposition rate of μc-Si:H and a-SiGe:H films with high uniformity. The μc-Si:H is deposited with pure SiH_4, microstructure started to form at 150 ºC with crystallinity 59% for 300nm thick film. The deposition rate is as high as 5 Å/s with crystallinity 68%, and 6.2 Å/s with crystallinity 45% on a 4 inch glass substrate. Moreover, a thin incubation layer has formed near substrate and film became fully dense conical conglomerates at 300nm since the crystalline fraction for 35nm film is 44%, 69% for 300nm film, 70% for 1μm film. The crystal orientations are Si(111), Si(220) and Si(311) determined by XRD. In addition, a-SiGe:H has been tried with modified ICP-CVD system. Energy bandgap has been adjusted by changing SiH_4-to-GeH_4 ratio from 1.25 to 1.63eV. Also, microcrystalline structure appears in Si-rich region.

Heterojunction solar cells have been deposited by films developed in this thesis. Interference fringes have been observed in EQE spectra on smooth substrate, which can be avoided by using textured substrate. The HIT cell shows good EQE spectra with maximum 86% around 700µm wavelength. The effect of intrinsic layer thickness has been studied and the optimum thickness is 15nm in this thesis. Moreover, dark I-V curve has been characterized. It's suspected that Schottky diode has formed between emitter and metal contacts, which caused a kink in the fourth quadrant of I-V curve

Bibliography

[1] Energy research Centre of the Netherlands (ECN), Policy Studies, "Solar PV," .

[2] European Photovoltaic Industry Association, "Global market outlook for photovoltaics until 2014," *Accessed November,* vol. 16, pp. 2011, 2011.

[3] S. Mehta, "PV News Annual Data Collection Results: 2010 Cell, Module Production Explodes Past 20 GW---Technology trends, competitive dynamics, top producers, and the outlook for 2011," May 09, 2011.

[4] J. Poortmans and V. Arkhipov, *Thin Film Solar Cells: Fabrication, Characterization and Applications.* Wiley, 2006.

[5] Anonymous "Plams-enhanced chemical vapor deposition," October 17, 2012, .

[6] K. L. Chopra, "Thin film solar cells (A status review)," in *PVTC 2011,* Southern France, 2011, .

[7] K. Yamamoto, A. Nakajima, M. Yoshimi, T. Sawada, S. Fukuda, T. Suezaki, M. Ichikawa, Y. Koi, M. Goto and T. Meguro, "A thin-film silicon solar cell and module," *Prog Photovoltaics Res Appl,* vol. 13, pp. 489-494, 2005.

[8] J. Bailat, L. Fesquet, J. B. Orhan, Y. Djeridane, B. Wolf, P. Madliger, J. Steinhauser, S. Benagli, D. Borrello and L. Castens, "Recent developments of high-efficiency micromorph® tandem solar cells in kai-M PECVD reactors," in *Proc. 25th Eur. Photovoltaic Solar Energy Conf./5th World Conf. Photovoltaic Energy Convers,* 2010, pp. 2720-2723.

[9] J. Yang and S. Guha, "Status and future perspective of a-Si: H, a-SiGe: H, and nc-Si: H thin film photovoltaic technology," *AE Delahoy, LA Eldada, Thin Film Solar Technology, Proceedings of the SPIE,* vol. 7409, pp. 74090C1À74090C14, 2009.

[10] M. A. Green, K. Emery, Y. Hishikawa, W. Warta and E. D. Dunlop, "Solar cell efficiency tables (version 39)," *Prog Photovoltaics Res Appl,* vol. 20, pp. 12-20, 2012.

[11] M. L. Terry, *Post–deposition Processing of Polycrystalline Silicon thin–film Solar Cells on low–temperature Glass Superstrates,* 2007.

[12] G. Overton, "CdTe photovoltaic solar-cell efficiency record of 17.3% set by First Solar," 07/29/2011, .

[13] M. Osborne, "DuPont enabling new market opportunities for CdTe thin film manufacturers," June 02, 2011, .

[14] A. Romeo, M. Arnold, D. Bätzner, H. Zogg and A. Tiwari, "Development of high efficiency flexible CdTe solar cells," in *Proceedings of PV in Europe from PV Technology to Energy Solutions Conference and Exhibition, Rome, Italy,* 2002, pp. 377-381.

[15] I. Matulionis, S. Han, J. A. Drayton, K. J. Price and A. D. Compaan, "Cadmium telluride solar cells on molybdenum substrates," in *MRS Proceedings,* 2001, .

[16] I. Repins, M. Contreras, M. Romero, Y. Yan, W. Metzger, J. Li, S. Johnston, B. Egaas, C. DeHart and J. Scharf, "Characterization of 19.9%-efficient CIGS absorbers," in *Photovoltaic Specialists Conference, 2008. PVSC'08. 33rd IEEE,* 2008, pp. 1-6.

[17] L. Hughes, "Stion Sets New Efficiency High of 14.8% for Monolithic CIGS Module in Production," June 12, 2012, .

[18] E. Wesoff, "Stion Ups Efficiency for CIGS Solar Panels, Plus Recent PV Performance Records**,**" June 22, 2012, .

[19] M. Marcus, "MiaSole Sets Flexible PV Efficiency World Record at 15.5 Percent," May 24, 2012, .

[20] NANOCO Group PLC, "Capturing energy," .

[21] M. W. Rowell and M. D. McGehee, "Transparent electrode requirements for thin film solar cell modules," *Energy & Environmental Science,* vol. 4, pp. 131-134, 2011.

[22] International Solar Electric Technology (ISET), "Thechnology overview," .

[23] A. G. Aberle, "Thin-film solar cells," *Thin Solid Films,* vol. 517, pp. 4706-4710, 2009.

[24] Oxford Instrument Plasma Technology, "Plasma Enhanced Chemical Vapour Deposition (PECVD)," .

[25] M. Otobe and S. Oda, "Preparation of microcrystalline silicon films by very-high-frequency digital chemical vapor deposition," *Japanese Journal of Applied Physics,* vol. 31, pp. 1948-1952, 1992.

[26] H. Mashima, H. Yamakoshi, K. Kawamura, Y. Takeuchi, M. Noda, Y. Yonekura, H. Takatsuka, S. Uchino and Y. Kawai, "Large area VHF plasma production using a ladder-shaped electrode," *Thin Solid Films,* vol. 506, pp. 512-516, 2006.

[27] A. Mahan, Y. Xu, E. Iwaniczko, D. Williamson, B. Nelson and Q. Wang, "Amorphous silicon films and solar cells deposited by HWCVD at ultra-high deposition rates," *J. Non Cryst. Solids,* vol. 299, pp. 2-8, 2002.

[28] G. Neudeck and A. Malhotra, "Field effect conductance modulation in vacuum-evaporated amorphous silicon films," *J. Appl. Phys.,* vol. 46, pp. 239-246, 1975.

[29] R. M. Robertson and M. J. Rossi, "Sticking coefficient of the SiH 2 free radical on a hydrogenated silicon-carbon surface," *Appl. Phys. Lett.,* vol. 54, pp. 185-187, 1989.

[30] R. A. Street, *Hydrogenated Amorphous Silicon.* Cambridge University Press, 2005.

[31] S. Wieder and F. Jülich, *Amorphous Silicon Solar Cells: Comparison of Pin and Nip Structures with Zinc Oxide Frontcontact,* 1999.

[32] S. Veprek, Z. Iqbal, H. Oswald and A. Webb, "Properties of polycrystalline silicon prepared by chemical transport in hydrogen plasma at temperatures between 80 and 400 degrees C," *Journal of Physics C: Solid State Physics,* vol. 14, pp. 295, 2000.

[33] J. Perrin and T. Broekhuizen, "Surface reaction and recombination of the SiH< inf> 3</inf> radical on hydrogenated amorphous silicon," *Appl. Phys. Lett.,* vol. 50, pp. 433-435, 1987.

[34] P. Ho, W. G. Breiland and R. J. Buss, "Laser studies of the reactivity of SiH with the surface of a depositing film," *J. Chem. Phys.,* vol. 91, pp. 2627, 1989.

[35] S. Yamasaki, U. K. Das, T. Umeda, J. Isoya and K. Tanaka, "Creation and annihilation mechanism of dangling bonds within the a-Si: H growth surface studied by in situ ESR technique," *J. Non Cryst. Solids,* vol. 266, pp. 529-533, 2000.

[36] B. Landkammer, A. Von Keudell and W. Jacob, "Erosion of thin hydrogenated carbon films in oxygen, oxygen/hydrogen and water plasmas," *J. Nucl. Mater.,* vol. 264, pp. 48-55, 1999.

[37] P. Capezzuto and A. Madan, *Plasma Deposition of Amorphous Silicon-Based Materials.* Academic Press, 1995.

[38] S. Vepřek and V. Mareček, "The preparation of thin layers of Ge and Si by chemical hydrogen plasma transport," *Solid-State Electronics,* vol. 11, pp. 683-684, 1968.

[39] A. Matsuda, "Growth mechanism of microcrystalline silicon obtained from reactive plasmas," *Thin Solid Films,* vol. 337, pp. 1-6, 1999.

[40] E. Fathi, "Thin Film Solar Cells on Transparent Plastic Foils," 2011.

[41] A. H. M. Smets, C. Smit, W. Kessels and M. van den Sanden, *Growth Related Material Properties of Hydrogenated Amorphous Silicon.* Technische Universiteit Eindhoven, 2002.

[42] E. Vallat-Sauvain, U. Kroll, J. Meier, A. Shah and J. Pohl, "Evolution of the microstructure in microcrystalline silicon prepared by very high frequency glow-discharge using hydrogen dilution," *J. Appl. Phys.,* vol. 87, pp. 3137-3142, 2000.

[43] C. Tsai, J. Knights, G. Chang and B. Wacker, "Film formation mechanisms in the plasma deposition of hydrogenated amorphous silicon," *J. Appl. Phys.,* vol. 59, pp. 2998-3001, 1986.

[44] S. Filonovich, H. Aguas, I. Bernacka-Wojcik, C. Gaspar, M. Vilarigues, L. Silva, E. Fortunato and R. Martins, "Highly conductive p-type nanocrystalline silicon films deposited by RF-PECVD using silane and trimethylboron mixtures at high pressure," *Vacuum,* vol. 83, pp. 1253-1256, 2009.

[45] R. Swanepoel, "Determination of the thickness and optical constants of amorphous silicon," *Journal of Physics E: Scientific Instruments,* vol. 16, pp. 1214, 2000.

[46] W. Lodders, "Powder formation in silane plasma's." *Appl.Phys,* vol. 79, pp. 1303, 1996.

[47] K. E. Balish, T. Nowak, T. Tanaka and M. Beals, *Dilute Remote Plasma Clean,* 2001.

[48] A. Gupta, *Decontamination of a Plasma Reactor using a Plasma After a Chamber Clean,* 1998.

[49] L. Williams, D. R. Pirkle, W. Harshbarger and T. Ebel, *Plasma Cleaning Method for Removing Residues in a Plasma Process Chamber,* 1997.

[50] Oxford Instrument Plasma Technology, "Basic PECVD plasma processes (SiH4 based)----- oxford instrument plasma technology," 2003.

[51] D. Han, K. Wang, J. M. Owens, L. Gedvilas, B. Nelson, H. Habuchi and M. Tanaka, "Hydrogen structures and the optoelectronic properties in transition films from amorphous to microcrystalline silicon prepared by hot-wire chemical vapor deposition," *J. Appl. Phys.,* vol. 93, pp. 3776-3783, 2003.

[52] M. Tucci, "Optimization of n-doping in n-type a-SI: H/p-type textured c-Si heterojunction for photovoltaic applications," *Solar Energy Mater. Solar Cells,* vol. 57, pp. 249-257, 1999.

[53] T. Dylla, *Electron Spin Resonance and Transient Photocurrent Measurements on Microcrystalline Silicon.* Forschungszentrum, Zentralbibliothek, 2005.

[54] H. Richter, Z. Wang and L. Ley, "The one phonon Raman spectrum in microcrystalline silicon," *Solid State Commun,* vol. 39, pp. 625-629, 1981.

[55] R. Kobliska and S. Solin, "Raman spectrum of wurtzite silicon," *Physical Review B,* vol. 8, pp. 3799-3802, 1973.

[56] R. Tsu, J. Gonzalez-Hernandez, S. Chao, S. Lee and K. Tanaka, "Critical volume fraction of crystallinity for conductivity percolation in phosphorus-doped Si: F: H alloys," *Appl. Phys. Lett.,* vol. 40, pp. 534, 1982.

[57] E. Edelberg, S. Bergh, R. Naone, M. Hall and E. S. Aydil, "Luminescence from plasma deposited silicon films," *J. Appl. Phys.,* vol. 81, pp. 2410-2417, 1997.

[58] P. Torres, J. Meier, R. Fluckiger, U. Kroll, J. A. Selvan, H. Keppner, A. Shah, S. Littelwood, I. Kelly and P. Giannoules, "Device grade microcrystalline silicon owing to reduced oxygen contamination," *Appl. Phys. Lett.,* vol. 69, pp. 1373-1375, 1996.

[59] X. Jiang, Y. He and H. Zhu, "The effect of passivation of boron dopants by hydrogen in nano-crystalline and micro-crystalline silicon films," *Journal of Physics: Condensed Matter,* vol. 6, pp. 713, 1999.

[60] P. Luo, Z. Zhou, K. Chan, D. Tang, R. Cui and X. Dou, "Gas doping ratio effects on p-type hydrogenated nanocrystalline silicon thin films grown by hot-wire chemical vapor deposition," *Appl. Surf. Sci.,* vol. 255, pp. 2910-2915, 2008.

[61] Y. Sobajima, S. Kamanaru, H. Muto, J. Chantana, C. Sada, A. Matsuda and H. Okamoto, "Effect of thermal annealing and hydrogen-plasma treatment in boron-doped microcrystalline silicon," *J. Non Cryst. Solids,* 2011.

[62] G. Lihui and L. Rongming, "Studies on the formation of microcrystalline silicon with PECVD under low and high working pressure," *Thin Solid Films,* vol. 376, pp. 249-254, 2000.

[63] J. Rath and R. Schropp, "Incorporation of p-type microcrystalline silicon films in amorphous silicon based solar cells in a superstrate structure," *Solar Energy Mater. Solar Cells,* vol. 53, pp. 189-203, 1998.

[64] R. Ramesham, "Effect of annealing and hydrogen plasma treatment on the voltammetric and impedance behavior of the diamond electrode," *Thin Solid Films,* vol. 315, pp. 222-228, 1998.

[65] K. Tanaka, *Glow-Discharge Hydrogenated Amorphous Silicon.* Kluwer Academic Pub, 1989.

[66] B. Strahm, A. Howling, L. Sansonnens, C. Hollenstein, U. Kroll, J. Meier, C. Ellert, L. Feitknecht and C. Ballif, "Microcrystalline silicon deposited at high rate on large areas from pure silane with efficient gas utilization," *Solar Energy Mater. Solar Cells,* vol. 91, pp. 495-502, 2007.

[67] H. Fujiwara, M. Kondo and A. Matsuda, "Real-time spectroscopic ellipsometry studies of the nucleation and grain growth processes in microcrystalline silicon thin films," *Physical Review B,* vol. 63, pp. 115306, 2001.

[68] M. N. van den Donker and F. Jülich, *Plasma Deposition of Microcrystalline Silicon Solar Cells: Looking Beyond the Glass.* Forschungszentrum Jülich GmbH, Zentralbibliothek, 2006.

[69] M. Goto, H. Toyoda, M. Kitagawa, T. Hirao and H. Sugai, "Low temperature growth of amorphous and polycrystalline silicon films from a modified inductively coupled plasma," *Japanese Journal of Applied Physics,* vol. 36, pp. 3714-3720, 1997.

[70] M. Van den Donker, B. Rech, F. Finger, L. Houben, W. Kessels and M. Van de Sanden, "Deposition of highly efficient microcrystalline silicon solar cells under conditions of low H2 dilution: the role of the transient depletion induced incubation layer," *Prog Photovoltaics Res Appl,* vol. 15, pp. 291-301, 2007.

[71] B. Yan, L. Zhao, B. Zhao, J. Chen, G. Wang, H. Diao, Y. Mao and W. Wang, "Hydrogenated amorphous silicon germanium alloy with enhanced photosensitivity prepared by plasma enhanced chemical vapor deposition at high temperature," *Vacuum,* 2012.

[72] Q. H. Fan, C. Chen, X. Liao, X. Xiang, S. Zhang, W. Ingler, N. Adiga, Z. Hu, X. Cao and W. Du, "High efficiency silicon–germanium thin film solar cells using graded absorber layer," *Solar Energy Mater. Solar Cells,* vol. 94, pp. 1300-1302, 2010.

[73] F. J. Kampas, "Chemical reactions in plasma deposition," *Semiconductors and Semimetals,* vol. 21, pp. 153-177, 1984.

[74] J. Souhabi, V. Torres, A. Postnikov and K. Rustagi, "Re-examination of the SiGe Raman spectra-Linear chain approximation and ab initio calculations," *ArXiv Preprint arXiv:1109.6585,* 2011.

[75] G. Adamopoulos, J. Robertson, N. Morrison and C. Godet, "Hydrogen content estimation of hydrogenated amorphous carbon by visible Raman spectroscopy," *J. Appl. Phys.,* vol. 96, pp. 6348-6352, 2004.

[76] S. Hegedus, R. Rocheleau, R. Tullman, D. Albright, N. Saxena, W. Buchanan, K. Schubert and R. Dozier, "Photo-assisted CVD of a-si: H solar cells and a-SiGe: H films," in *Photovoltaic Specialists Conference, 1988., Conference Record of the Twentieth IEEE,* 1988, pp. 129-134.

[77] T. J. King and K. C. Saraswat, "Deposition and Properties of Low-Pressure Chemical-Vapor Deposited Polycrystalline Silicon-Germanium Films," *J. Electrochem. Soc.,* vol. 141, pp. 2235-2241, 1994.

[78] X. Liao, H. Povolny, P. Agarwal and X. Deng, "Raman and IR study of narrow bandgap A-sige and μC-SiGe films deposited using different hydrogen dilution," in *Photovoltaic Specialists Conference, 2002. Conference Record of the Twenty-Ninth IEEE,* 2002, pp. 1150-1153.

[79] A. Matsuda, "Amorphous Si and Si-based alloys from glow-discharge plasma," *Pure & Appl.Chem,* vol. 60, pp. 733-740, 1988.

[80] T. Karabacak, Y. P. Zhao, G. C. Wang and T. M. Lu, "Growth front roughening in silicon nitride films by plasma-enhanced chemical vapor deposition," *Physical Review B,* vol. 66, pp. 075329, 2002.

[81] S. Hazra, A. Middya, S. Ray, C. Malten and F. Finger, "Role of deposition parameters on the photovoltaic quality of amorphous silicon germanium alloys: correlation of microstructure with defect density and electronic transport," *J. Phys. D,* vol. 34, pp. 2475, 2001.

[82] M. I. Alonso and K. Winer, "Raman spectra of c-Si_ {1-x} Ge_ {x} alloys," *Physical Review B,* vol. 39, pp. 10056, 1989.

[83] R. Hübner, H. J. Engelmann and E. Zschech, "Challenges to quantitative energy-dispersive X-ray spectrometry and its application to graded embedded silicon–germanium for high-performance complementary metal oxide semiconductor devices," *Thin Solid Films,* vol. 519, pp. 203-209, 2010.

[84] W. Luft, "Characteristics of hydrogenated amorphous silicon-germanium alloys," in *Photovoltaic Specialists Conference, 1988., Conference Record of the Twentieth IEEE,* 1988, pp. 218-223.

[85] S. Jones, Y. Chen, D. Williamson, R. Zedlitz and G. Bauer, "Microstructural transition and degraded opto-electronic properties in amorphous SiGe: H alloys," *Appl. Phys. Lett.,* vol. 62, pp. 3267-3269, 1993.

[86] A. Skumanich, A. Frova and N. Amer, "Urbach tail and gap states in hydrogenated a-SiC and a-SiGe alloys," *Solid State Commun,* vol. 54, pp. 597-601, 1985.

[87] M. Zeman and D. Zhang, "Heterojunction silicon based solar cells," *Physics and Technology of Amorphous-Crystalline Heterostructure Silicon Solar Cells,* pp. 13-43, 2011.

[88] B. Hekmatshoar, D. Shahrjerdi and D. K. Sadana, "Novel heterojunction solar cells with conversion efficiencies approaching 21% on p-type crystalline silicon substrates," in *Electron Devices Meeting (IEDM), 2011 IEEE International,* 2011, pp. 36.6. 1-36.6. 4.

[89] M. Schmidt, L. Korte, A. Laades, R. Stangl, C. Schubert, H. Angermann, E. Conrad and K. Maydell, "Physical aspects of a-Si: H/c-Si hetero-junction solar cells," *Thin Solid Films,* vol. 515, pp. 7475-7480, 2007.

[90] Q. Wang, M. Page, E. Iwaniczko, Y. Xu, L. Roybal, R. Bauer, B. To, H. C. Yuan, A. Duda and F. Hasoon, "Efficient heterojunction solar cells on< equation> p</equation>-type crystal silicon wafers," *Appl. Phys. Lett.,* vol. 96, pp. 013507-013507-3, 2010.

[91] Y. C. Lin, Y. Jian and J. Jiang, "A study on the wet etching behavior of AZO (ZnO: Al) transparent conducting film," *Appl. Surf. Sci.,* vol. 254, pp. 2671-2677, 2008.

[92] J. Löffler, A. Gordijn, R. Stolk, H. Li, J. Rath and R. Schropp, "Amorphous and 'micromorph'silicon tandem cells with high open-circuit voltage," *Solar Energy Mater. Solar Cells,* vol. 87, pp. 251-259, 2005.

[93] R. Hussein, D. Borchert, G. Grabosch and W. Fahrner, "Dark I–V–T measurements and characteristics of (n) a-Si/(p) c-Si heterojunction solar cells," *Solar Energy Mater. Solar Cells,* vol. 69, pp. 123-129, 2001.

[94] M. Glatthaar, M. Riede, N. Keegan, K. Sylvester-Hvid, B. Zimmermann, M. Niggemann, A. Hinsch and A. Gombert, "Efficiency limiting factors of organic bulk heterojunction solar cells identified by electrical impedance spectroscopy," *Solar Energy Mater. Solar Cells,* vol. 91, pp. 390-393, 2007.

[95] W. Zhu, T. P. Ma, T. Tamagawa, J. Kim and Y. Di, "Current transport in metal/hafnium oxide/silicon structure," *Electron Device Letters, IEEE,* vol. 23, pp. 97-99, 2002.

[96] B. Van Zeghbroeck, "Principles of semiconductor devices," *Colorado University,* 2004.

[97] B. Rezek, T. Mates, J. Kocka and A. Stemmer, "Charge storage in undoped hydrogenated amorphous silicon by ambient atomic force microscopy," *Appl. Phys. Lett.,* vol. 83, pp. 1764-1766, 2003.

[98] R. A. Street, "Doping and the Fermi energy in amorphous silicon," *Phys. Rev. Lett.,* vol. 49, pp. 1187-1190, 1982.

[99] Anonymous "http://environmentalchemistry.com/yogi/periodic/Ti.html," .

[100] C. Y. Chen, K. Y. Wu, Y. C. Chao, H. W. Zan, H. F. Meng and Y. T. Tao, "Concomitant tuning of metal work function and wetting property with mixed self-assembled monolayers," *Organic Electronics,* vol. 12, pp. 148-153, 2011.

[101] P. Anderson, "Model for the electronic structure of amorphous semiconductors," *Phys. Rev. Lett.,* vol. 34, pp. 953-955, 1975.

[102] Q. Feng, W. Wang, K. Jiang, J. Huang, Y. Zhang, W. Song and R. Tan, "Effect of deposition condition and UV-ozone post-treatment on work function of DC magnetron sputtered AZO thin films," *J. Mater. Sci. : Mater. Electron.,* vol. 23, pp. 267-272, 2012.